Rheology of Polyelectrolyte Multilayer Modified Suspensions

A dissertation submitted to the

PHD Program Polymer Science

Bayreuth Graduate School of Mathematical and Natural Sciences

University of Bayreuth

for the degree

Doctor of Natural Sciences (Dr. rer. nat.)

presented by

Andreas Hess

September, 2012

Die vorliegende Arbeit wurde in der Zeit von August 2008 bis September 2011 in Bayreuth am Lehrstuhl Technische Mechanik und Strömungsmechanik unter Betreuung von Herrn Prof. Dr.Nuri Aksel angefertigt.

Vollständiger Abdruck der von der Bayreuther Graduiertenschule für Mathematik und Naturwissenschaften der Universität Bayreuth genehmigten Dissertation zur Erlangung des akademischen Grades eines Doktors der Naturwissenschaften (Dr. rer. nat.).

Promotionsgesuch eingereicht am:	21. September 2012
Zulassung durch das Leitungsgremium:	15. Oktober 2012
Wissenschaftliches Kolloquium:	23. April 2013

Amtierender Direktor der Graduiertenschule: Prof. Dr. Franz X. Schmid

Prüfungsausschuss:	Prof. Dr. Nuri Aksel	(Erstgutachter)
	Prof. Dr. Stephan Förster	(Zweitgutachter)
	Prof. Dr. Volker Altstädt	(Vorsitz)
	Prof. Dr. Andreas Fery	

Abstract / Zusammenfassung

Abstract

In the last two decades, the tuning of soft materials' properties has reached more and more technological and scientific significance. A wealth of new colloidal systems emerged from the need of soft materials with well-defined, and adjustable, rheological properties. Prominent examples are multiarm star polymers, microgels, thermosensitive colloids, and depletion gels. These systems are tailored to correlate microscopic interactions with macroscopic behavior, which is poorly understood for complex systems. The interparticle interactions are controlled at the synthesis level or strongly coupled to the background fluid. This is a serious drawback of the established colloidal systems. What lacks is a colloidal system that combines high flexibility in changing the tuning parameters with fast and cost effective production. Self-assembled polyelectrolyte multilayer modified colloids are a relatively new and promising colloidal system that is expected to overcome the previous mentioned drawbacks of the established systems.

For the first time, this thesis explores the micro-macro interactions of polyelectrolyte mutlilayer (PEM) modified colloids. Thereby, the focus lies on dense colloidal suspensions for which the individual motion of single particles is strongly restricted by the neighboring particles. Then, the suspensions show simultaneously elastic and viscous properties with dominating solid-like behavior at rest, and yield and flow under large applied stresses.

The first experiments of this thesis investigate the effect of the layer number on rheology. At low layer numbers, the rheology suffers from an inhomogeneous PEM surface which introduces localized attractions to the suspensions. This results in a more brittle material as the local attractions are strong in radial direction, but easily break down under lateral shear – a mechanism that is similar to a fridge magnet sticker. In rheology, this behavior becomes apparent when the yield stress, as the measure for the equilibrium stress scale, is compared to the elasticity of the equilibrium microstructure. The ratio of yield stress to elasticity decreases with increasing layer number and reaches a plateau for high layer numbers where the PEM

surface is well-defined. This finding gives a first guideline for the estimation of the precursor regime with macroscopic tools. Another remarkable result was the finding that the rheology is governed by the kind of terminating polyelectrolyte of the PEM film.

The role of the layer number and the terminating polyelectrolyte were investigated in a second set of experiments, thereby focusing on the rheology at high shear stresses. At high shear stresses, dense suspensions are expected to shear thicken. That is, their viscosity increases with shear stress. The transition from Newtonian flow at medium shear stress to shear thickening is a very sensitive measure for the relevant forces that govern the rheology, and hence the experiments identify that at high shear stresses hydrodynamic forces dominate the interparticle interactions. Moreover, the strength of the hydrodynamic force depends again on the terminating polyelectrolyte and is due to the specific porosity of the PEM film.

Following experiments investigated the role of the terminating polyelectrolyte in more detail. Systematic variation of the polyelectrolyte conformation and the ionic strength of the background fluid showed that the terminating polyelectrolyte behaves similar to polyelectrolyte brushes. This finding gives rise to the assumption that terminating polyelectrolyte acts like a hairy layer and the particles can be seen as hairy core-shell particles, which share some properties with multiarm star polymers.

Zusammenfassung

In den letzten zwei Jahrzehnten hat das gezielte Einstellen der Eigenschaften von weicher Materie mehr und mehr technologische und wissenschaftliche Bedeutung erreicht. Aus dem Bedürfnis nach weicher Materie mit definierten und einstellbaren rheologische Eigenschaften, entstand eine Fülle neuer kolloidaler Systeme. Prominente Beispiele sind Multiarm - Sternpolymere, Mikrogele, temperatursensitive Kolloide, und kolloidale Gele. Diese Systeme sind darauf maßgeschneidert die, für solch komplexe Materialien ungenügend verstandene, Korrelation der mikroskopischen Wechselwirkungen mit ihrem makroskopische Materialverhalten zu untersuchen. Die Wechselwirkungen zwischen den Partikeln werden durch die chemische Synthese kontrolliert oder sind stark mit dem Dispersionsmedium gekoppelt. Dies ist ein schwerwiegender Nachteil der etablierten kolloidalen Systemen. Wünschenswert wäre ein kolloidales System, das eine hohe Flexibilität bei der Änderung der Einstell-Parameter mit einer schnellen und kostengünstigen Produktion vereint. Polyelektrolytmultlagen modifizierte Kolloide sind eine relativ neues und vielversprechendes kolloidales System, von dem erwartet wird, dass es die vorher genannten Nachteile der etablierten Systeme überwinden kann.

Zum ersten Mal untersucht diese Arbeit die Mikro - Makro - Wechselwirkungen von mit Polyelektrolyt Mutlilagen (PEM) modifizierten Kolloiden. Dabei liegt der Fokus auf dichten kolloidalen Suspensionen, für die die Bewegung einzelner Partikel stark von den benachbarten Partikeln eingeschränkt wird. Dann zeigen die Suspensionen gleichzeitig elastische und viskose Eigenschaften, mit dominierendem festkörperartigem Verhalten in Ruhe, einer Fließgrenze, und dominierendem fluidartigem Verhalten bei großen Belastungen.

Die ersten Experimente in dieser Arbeit untersuchen die Auswirkungen der Lagenanzahl der PEMs auf das rheologische Verhalten der Suspensionen. Bei wenigen Lagen Polyelektrolyt, werden die rheologischen Eigenschaften von der inhomogenen PEM Oberfläche, und den daraus resultierenden lokalen Wechselwirkungskräften, bestimmt. Die Suspensionen verhälten sich spröde, was darauf zurückzuführen ist, dass die lokalen Wechselwirkungskräfte in radialer Richtung zwar stark sind, unter einer Scherbeanspruchung aber leicht überwunden werden können. Dieses Verhalten kennt man von Kühlschrank Magneten. In dem rheologischen Verhalten, zeigt sich dieser Effekt, wenn man die Scherkräft an der Fließgrenze mit den elastischen Kräften der Mikrostruktur vergleicht. Das Verhältnis von Fließgrenze zu Elastizität nimmt mit zunehmender Anzahl an Polymer Lagen ab, und erreicht einen konstanten Wert wenn die PEM Oberfläche sehr homogen ist. Dieses Ergebnis gibt einen ersten Anhaltspunkt wie sich die Mindestanzahl an Polyelektrolyt Lagen für die Herstellung reproduzierbarer Kolloide mit makroskopischen Methoden abschätzen lässt. Ein weiteres bemerkenswertes Ergebnis war die Feststellung, dass das Fließverhalten wesentlich durch die äußerste Polyelektrolyt Lage des Multilagen Films bestimmt wird.

Die Rolle der Anzahl an Polyelektrolyt Lagen, und der äußersten Polyelektrolyt Lage wurde in weiteren Experimenten näher untersucht. Dabei lag der Schwerpunkt auf dem rheologis-

chen Verhalten bei großer Scherung. Bei großen Scherspannungen wird bei dichten Suspensionen Scherverdickung, also eine Zunahme der Viskosität mit der Scherspannung, erwartet. Der Übergang von Newtonschen Fließen bei mittleren Scherspannung zu Scherverdickung bei großen Scherspannungen ist ein sehr empfindliches Maß für die wirkenden Kräfte die das rheologische Verhalten bestimmen. Die Versuche zeigten, dass bei großen Scherspannungen die hydrodynamischen Kräfte das rheologische Verhalten bestimmen. Wie stark die hydrodynamischen Kräfte sind, hängt von der äußersten Lage an Polyelektrolyt ab, und ist auf die jeweilige Porosität des Multilagen Films zurückzuführen.

Anschließende Experimenten untersuchten die Rolle der äußersten Polyelektrolyt Lage im Detail. Die systematischen Variation der Konformation der Polyelektrolyte während der PEM Herstellung, sowie die Variation der Ionenstärke des Dispersionsmediums zeigte, dass Kolloide mit Multilagen Filme aus bürstenartigen Polyelektrolyten eine höhere Fließgrenze aufweisen als solche aus langgestreckten Polyelektrolyten. Dieses Ergebnis gibt Anlass zu der Annahme, dass sich die äußerste Polyelektrolyt Lage wie eine haarige Schicht verhält und die Partikl als haarige Kern-Schale-Partikel mit ähnlichen Eigenschaften wie zum Beispiel Multiarm - Sternpolymere angesehen werden können.

Citations to Previously Published Work

Chapter 4 was published as:

"Yielding and Structural Relaxation in Soft Materials: Evaluation of Strain-Rate Frequency Superposition Data by Stress Decomposition Method," A. Hess, N. Aksel, Phys. Rev. E **84**, 051502 (2011).

Author contributions: Had the idea, carried out the experiments, analyzed the data,and wrote the manuscript.

Chapter 5 was published as the article:

"Systematic Modification of the Rheological Properties of Colloidal Suspensions with Polyelectrolyte Multilayers," A. Hess, M. Pretzl, L. Heymann, A. Fery, N. Aksel, Phys. Rev. E **84**, 031407 (2011).

Author contributions: Performed the rheological experiments and interpreted the data. Did the atomic force-imaging, processed the data, and wrote the manuscript.

Chapter 6 is from the manuscript:

"Impact of Brushy Polyelectrolyte Multilayers on Viscoelasticity in Dense Suspensions," A. Hess, N. Aksel, Soft Matter (submitted)

Author contributions: Developed the idea, carried out the experiments, analyzed the data, and wrote the manuscript.

Chapter 7 is from the manuscript:

"Yield Stress and Scaling of Polyelectrolyte Multilayer Modified Suspensions: Effect of Polyelectrolyte Conformation During Multilayer Assembly" A. Hess, N. Aksel, , Langmuir (under review)

Author contributions: Performed the experiments, analyzed the data, and wrote the manuscript.

Acknowledgements

For me, it is a great pleasure to acknowledge all the people that generously assisted me throughout the three years I worked in Bayreuth on this thesis.

First, and foremost, I thank my supervisors Professor Nuri Aksel and Professor Andreas Fery for their mentorship during – and beyond – the time of the thesis.

Professor Aksel gave me the freedom to develop my own ideas and helped putting them into practice. He had always time discussing the results and tirelessly helped structuring my ideas. Moreover, he supported my work with an excellent infrastructure.

Professor Fery introduced me to the field of micromechanics and colloid chemistry. I really enjoyed his enthusiasm for all scientific areas. He also provided an excellent infrastructure.

Besides their expertise, I learned a lot about organization and leadership from Professor Aksel and Professor Fery, and I always enjoyed being part of their research groups. Working as a part of these groups gave me the opportunity to interact with and learn from a lot of people of different disciplines. Few of them are: Professor Michael Borkovec, Melanie Pretzl, Markus Hundt, and Christoph Hanske, as well as Markus Horn, Marion Märkl, and Gabriele Jena.

This work would not have been possible without the assistance of Professor Hans-Werner Schmidt, who gave us access to his labs. I am grateful to Dr. Christian Neuber for puzzling out the synthesis recipe and patiently answering all of my questions concerning chemistry.

During my years in Bayreuth, I acknowledge funding by the Deutsche Forschungsgemeinschaft (DFG) through the Research Unit FG 608 "Nonlinear Dynamics of Complex Materials". Thanks to Professor Ingo Rehberg, who did a great job managing the Research Unit. He arranged a lot of inspiring talks and meetings which greatly broadened my horizon.

Discussions with Professor Markus Scholle, Dr. Ulrich Handge and Dr. Reinhardt Richter, were always stimulating. Their huge experience in their specific research fields, and their humor helped me a lot on my way to the completion of this thesis.

I am grateful to Katja Helmrich for her support and motivation during my time in Bayreuth.

Contents

1

Introduction

1.1 Polyelectrolyte Multilayer Modified Colloids

The tuning of the properties of soft materials has reached more and more technological and scientific significance. A wealth of new colloidal systems emerged from the need of soft materials with well-defined, and adjustable, rheological properties. Prominent examples are multiarm star polymers, microgels, thermosensitive colloids, and depletion gels. These systems are tailored to correlate microscopic interparticle interactions with macroscopic mechanical behavior. The interparticle interactions are controlled at the synthesis level or strongly coupled to the chemical composition of the background fluid. Each of the both points constitute a serious drawback of the before mentioned colloidal systems. What lacks is a colloidal system that combines high flexibility in changing the tuning parameters with fast and cost effective production. Self-assembled polyelectrolyte multilayer modified colloids are a relatively new and promising colloidal system that is expected to overcome the drawbacks of the established systems.

Immersing a charged colloid into an aqueous solution of oppositely charged polyelectrolytes (PEs) starts a self-assembly process that finishes with an adsorbed polyelectrolyte monolayer. This self-assembled monolayer reverses the surface charge of the colloidal template. Thereby, the surface charge is complexed with only a few per cent of the polyelectrolyte charges [1, 2]. Due to such charge overcompensation, an additional polyelectrolyte layer, which has to be oppositely charged again, can be subsequently adsorbed onto the self-assembled monolayer. Continuously repeated adsorption of alternating charged polyelectrolyte layers leads to nanometer-thin polyelectrolyte multilayer (PEM) films. This layer-by-layer (LbL) self-assemlby tech-

nique was invented in the 1990's and has now established itself as a versatile tool for PEM assembly [3, 4]. The LbL technique is even more important as the PEM films can be assembled onto templates of organic and a inorganic matter [5–8].

The thickness and roughness of a PEM film are strongly influenced by the salt concentration of the deposition solution; the higher the salt concentration the thicker and rougher are the PEM films. Typically, the thickness of a single PE layer is of the order of several nanometers. The underlying mechanism that dictates the thickness and roughness of the PEMs is the electrostatic screening due to counter ions of the dissolved salt. In salt free solution, the charged side groups of the PEs repel each other and the PE adopts its most elongated conformation, which results in reasonably smooth films. With increasing salt content, the screening increases and hence, the side groups converge and the PE adopts a brushy conformation. Especially when the polyelectrolytes adsorb in a brushy conformation, tails and loops from the terminating layer dangle into the surrounding background fluid. Hence, polyelectrolyte multilayer modification of colloids results in core-shell (flatly adsorbed PEs), or hairy core-shell (brushy adsorbed PEs) particles.

1.2 Dense Suspensions

In this thesis, we refer to dense suspensions as colloidal systems at high, typically $\phi > 0.4$, solid-to-liquid volume fractions. A good review of the rheology of dense suspension gives Stickel *et al.* in [9]. At this high volume fraction, the suspensions exist as amorphous materials. The amorphous microstructure, as exemplarily shown by Fig. 1.1, is the origin of quite remarkable features. At rest, the suspensions are jammed and behave solid-like, but yield and flow under an applied shear stress [10, 11]. For more than two decades, scientists are puzzled about this solid-to-liquid transition and nowadays it became evident that more effort has to be done in relating microscopic interparticle interactions to macroscopic material behavior [12–15].

Moreover, dense suspensions are ubiquitous in products of every day life, such as toothpaste, food products, paint, ink, ceramics [18, 19]. Considering their enormous economic significance as well as environmental aspects, it is of great practical interest to optimize the manufacturing processes of dense suspension based products. Such processes are dictated by the rheology of the specific suspension and hence it is crucial to tailor their mechanical behavior. This is typically done by nano scale tuning the interparticle interactions [20].

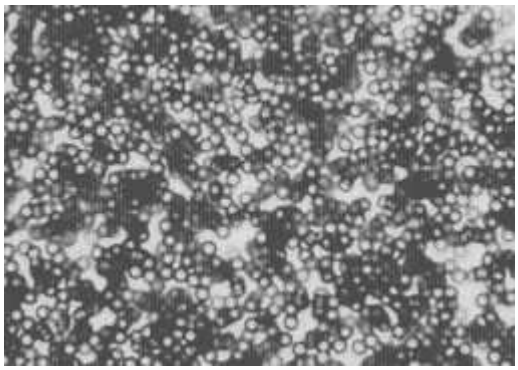

Figure 1.1: Amorphous microstructure of a dense suspension, $\phi = 0.4$, of unmodified colloids (radius 2.5 µm). The image was taken in a small gap shear cell [16, 17] after moderate shearing.

1.3 Thesis Outline

Using rheological methods, this thesis examines the macroscopic effects of polyelectrolyte multilayer modification to manufacture microscopically tunable dense colloidal suspensions. The thesis is composed of 7 chapters, where the first three chapters briefly introduce the motivation, measurement methods, and materials that build the basis of the thesis. The subsequent chapters are self-contained reports that may be read separately. They deal with the following micro-macro interactions:

- **Chap. 4: Yielding and Structural Relaxation in Soft Materials**

  Microscale: Material is characterized by structural disorder and metastability
  Macroscale: Material responds with ultra slow relaxation dynamics

- **Chap. 5: Systematic Modification of the Rheology of Dense Suspensions with PEMs**

  Microscale: Systematic variation of PEM film thickness as function of terminating polyelectrolyte
  Macroscale: i) Thin films (precursor regime) reveal ill-defined rheology, thick films (multilayer regime) rheologically are well-defined; ii) Terminating polyelectrolyte determines elastic modulus and yield stress

- **Chap. 6: Impact of Brushy PEMs on Viscoelasticity in Dense Suspensions**

  Microscale: Variation of terminating polyelectrolyte for brushy PEM films
  Macroscale: Yield stress, shear thickening, and viscoelasticity depend on the PEM termination

- **Chap. 7: Effect of polyelectrolyte conformation during multilayer assembly**

  Microscale: Systematic variation of PEM conformation (film roughness)
  Macroscale: Yield stress is a function of PEM conformation (film roughness)

2

Experimental Techniques

2.1 Rheology

Colloidal suspensions can be viscoelastic or viscoplastic. This means they exhibit liquid-like but also solid-like behaviour. Therefore, an important rheological feature is the yield stress that triggers the transition between liquid-like and solid-like behavior [21]. Several measures exist to characterize yield stress fluids. One of those measures is the static yield stress. In viscoelastic suspensions, the static yield stress is the maximum stress up to which the suspension elastically deforms. Above the static yield stress, the suspension irreversibly deforms and starts to flow. Besides the static yield stress there exists the concept of the dynamic yield stress [22]. In viscoplastic suspensions, the dynamic yield stress indicates the minimal (plateau) stress which is required to achieve a stable flow. This implies, that the dynamic yield stress is a function of the measurment time [23**?** –25]. Besides the yield stress, the most important measures are the viscosity and the elastic modulus, respectively describing the liquid-like and the solid-like properties. The reader can find a comprehensive introduction to the theory of viscoelasticity, for example, the textbook of Christensen [26].

In the following, we will introduce the rheological techniques that are used in this work. First, we focus on the standard techniques, which can be found in textbooks like that of Mezger [27], and afterwords, we switch to modern techniques that are just emerging.

2.1.1 Workhorse Techniques

Steady Shear Experiments

- **Strain-Rate Controled Measurements** – Strain-rate experiments with decreasing strain-rate $\dot{\gamma}$ and measured shear stress σ are suitable to determine the *dynamic* yield stress σ_{HB}. Transient experiments with increasing strain-rate and well-defined shear-time can serve to investigate static and dynamic yield stress. For this purpose, Heymann and Aksel [25] proposed a transient strain-rate ramp

$$\dot{\gamma}(t) = \dot{\gamma}_0 \left(\dot{\gamma}_\infty / \dot{\gamma}_0\right)^{t/\tau_r} , \tag{2.1}$$

  which naturally defines a characteristic shear-time per strain-rate step. This shear-time depends on the overall number of steps. In Eqn. (5.1) are $\dot{\gamma}_0$ and $\dot{\gamma}_\infty$ the initial and final strain-rates, respectively, and τ_r denotes the ramp-time.

- **Stress Controled Measurements** – During stress controled experiments, the shear stress σ is increased and the strain γ, as well as the strain-rate $\dot{\gamma}$, is recorded. At low stresses, the solid-like properties can be characterized by the elastic modulus $G = \sigma/\gamma$, whereas at high stresses the fluid-like properties are given by the viscosity $\eta = \sigma/\dot{\gamma}$. This type of measurement is appropriate to estimate the *static* yield stress σ_y.

Oscillatory Shear Experiments

- **Frequency Sweep Measurements** – In frequency sweeps, the strain amplitude γ_0 is kept fixed and the frequency ω decreases. These experiments are performed in the linear regime to ensure that $G'(\omega)$ and $G''(\omega)$ keep their physical meaning. Then, the frequency sweep gives the relaxation spectrum of the colloidal suspension.

- **Strain Sweep Measurements** – Strain sweep experiments are performed at fixed angular frequecy ω and increasing strain amplitude γ_0. During the strain sweeps, the elastic modulus $G'(\gamma_0)$ and the viscous modulus $G''(\gamma_0)$ are recorded. To estimate the limit of the linear regime, strain sweeps are commonly used as a prerequisite to frequency sweep measurements. It is worth to note that strain sweeps also serve to estimate the yield stress [28, 29].

2.1.2 Advanced Rheological Methods

The former introduced higher rheological data analysis techniques open up a door to new rheological methods. Two of them are used in this work, namely:

- **Constant-Rate Experiments** – Strain-rate sweep experiments are performed at a fixed strain-rate amplitude $\dot{\gamma}_0$. This can be achieved by increasing the strain amplitude γ_0 while the angular frequency ω decreases simultaneously. During the strain-rate sweeps, the elastic modulus $G'(\gamma_0, \omega)$ and the viscous modulus $G''(\gamma_0, \omega)$ are recorded.

- **Fourier-Transform Rheology** – At large strain amplitudes γ_0, the stress response, $\sigma_0(\gamma_0, \omega)$ is a function of strain, γ_0, and angular frequency, ω. With increasing strain and freuqency, the stress responds more and more non-linearly [30]. One common method to characterize non-linear rheology data, is to identify the higher harmonics of the stress signal using Fourier Analysis. This method has established as Fourier-Transform (FT) Rheology [31, 32].

- **Stress Decomposition Method** – A relatively new alternative method to deal with non-linear rheology data is the Stress Decomposition Method (SDM) [33]. The general idea behind the SDM is the decomposition of the stress response in an elastic and viscous part. Higher harmonics can be included in the analysis by Chebyshev polynomials of the first kind [34].

- **Strain-Rate Frequency Superposition** – Similar to the famous time-temperature superposition principle [21], the $G'(\gamma_0, \omega)$ and the $G''(\gamma_0, \omega)$ curves can be superposed onto a master curve [35]. The Strain-Rate Frequency Superposition (SRFS) is limited to linear rheology. This thesis extends the SRFS to non-linear rheology in Chap. 4.

2.2 Atomic Force Microscopy (AFM)

An atomic force microscope (AFM) can be used to image surface topographies within sub - nm resolution. The second main application field is the measurement of interaction forces between the probe and the sample. Hereby, the force resolution ranges from few pN to several nN. A recent review of the technique behind atomic force microscopy and its applications gives Butt et al. in [36], and so the following sections provide only the basis understanding.

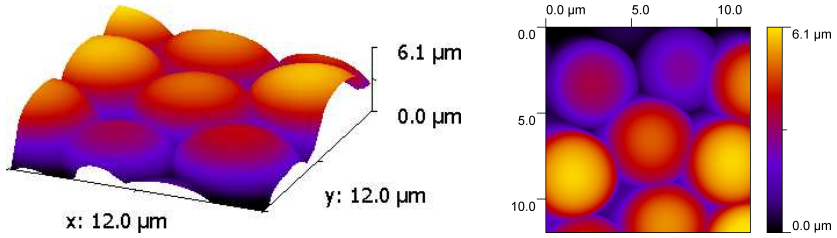

Figure 2.1: Cluster of polystyrene spheres, diameter 5 µm, imaged by using an atomic force microscope (AFM). The image to the right shows the same cluster but the image is flattened to obtain a 2 dimensional representation.

2.2.1 Basic Principles of AFM

The heart of an AFM is the probe, which can be a sharp tip, a colloid or even single molecules. The probe is located at the free end of a flexible cantilever. When the probe has contact with the sample or when it experiences attractive or repulsive interaction forces, it bends the cantilever. Then, the resulting cantilever deflection is measured by an optical device. The measured deflection can be further processed to obtain an image of an arbitrary sample topography or it is converted into a force measure.

2.2.2 AFM Imaging

The AFM images in this work, for an example see Fig. 2.1, are grabbed in the *intermittent contact mode*. In this mode, the cantilever tip oscillates with a frequency close to its resonance frequency (typically a few hundred kHz). The amplitude of the oscillation is set by the user and depends on the specific cantilever characteristics. The oscillating cantilever moves over the sample so that the tip makes contact with the sample only at maximum deflection. Then, a feedback loop permanently readjusts the amplitude. The adjusted length serves as a height measure for the topography of the sample. Close to contact, the oscillations are damped due to the stiffness of the sample or as a result of occuring adhesion forces. Therefore, the phase lag between the driving freqency and the measured oscillation frequency encodes information of the physicochemical surface properties of the sample.

The main advantage of this method is that the probe is only for a short time in contact with the sample which strongly reduces effects due to shearing the sample or tip abrasion.

2.3 Surface Charge and Particle Size Measurements

2.3.1 Zeta-Potential

The materials section will later on reveal that we deal with charged particles. In general, a charged solid surface that is immersed into an aqueous liquid is surrounded by several layers of liquid molecules and counter ions that adhere to the surface. Hence, when the solid moves, the shear plane is located at a distance δ away from the solid-liquid interface. The electric potential at the shear plane is defined as the zeta-potential, ζ. Throughout this thesis, the zeta-potential serves as a sufficiently good approximation of the surface charge of the colloids.

2.3.2 Electrophoresis for Zeta-Potential Measurement

It is relatively easy to estimate the zeta-potential using electrophoresis. Electrophoresis is the responding movement of a charged particle in an applied electric field. Thereby, the velocity of the particle, v, is proportional to the zeta-potential, $v \propto \zeta$, with the proportionality constant as a function of permittivity, electric field strength and inverse dynamic viscosity. The zeta-potential is estimated from the measured v. In this thesis, zeta-potential measurements are performed on a Nanosizer ZS (Malvern). This device uses a patented laser interferometric technique called M3-PALS (Phase Analysis Light Scattering) to determine the particle velocity as a function of the applied field.

The assumptions for the validity of the zeta-potential are (i), the electric double layer is not disturbed through the relative movement of the particle and the Poisson-Boltzmann equation is valid, and (ii), the electric field is homogeneous and not disturbed by the charged particle. Please find a more detailed discussion of charged surfaces and the resulting electrostatics in standard textbooks [37, 38] and recent reviews [39]. To match these conditions, there exists an optimum particle concentration for electrophoresis, which is determined by successively diluting a master suspension. The zeta-potential is estimated for each concentration of the serial dilution as depicted in Fig. 2.2.

2.3.3 Dynamic Light Scattering For Particle Size Measurement

In this thesis, particle size measurements are performed on a Mastersizer 2000 (Malvern). In this device, particles pass through the focus of a laser beam and the scattered light is evaluated. The Mastersizer uses the Mie scattering model which enables the device to measure particle

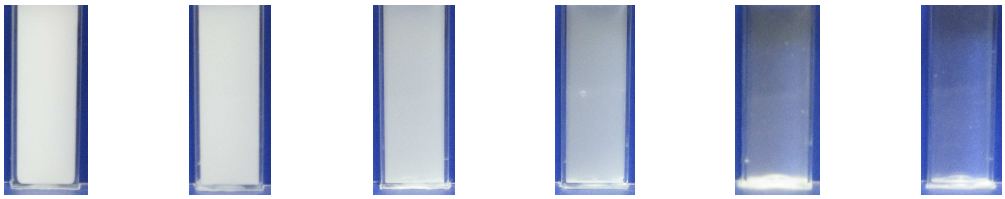

(a) 10^{-1} (b) $5 \cdot 10^{-2}$ (c) 10^{-2} (d) $5 \cdot 10^{-3}$ (e) 10^{-3} (f) $5 \cdot 10^{-4}$

Figure 2.2: Serial dilution for measuring the zeta potential. The given values denote the particle concentration in mol/L. The optimum particle concentration is at about 10^{-3} mol/L, picture (e).

sizes in the micron range. In the Mie scattering model, the scattering angle, θ, is inversely proportional to the particle radius, $\theta^{-1} \propto a$. The literature provides a detailed theory on the Mie scattering model [40, 41]

3

Polyelectrolyte Multilayer Modified Colloids

3.1 Polyelectrolyte Multilayers (PEMs)

Polyelectrolyte multilayers can be built from a wide variety of polyelectrolytes. The literature provides several recent reviews [4, 42, 43]. Since the aim of the thesis is to study the effect of PEM specific phenomena on the rheology of dense suspensions, throughout the thesis, a single polyanion/polycation pairing is used, namely (PDADMAC/PSS). This is one of the most studied polyelectrolyte complexes, where the both polyelectrolytes, poly(diallyldimethylammonium chloride) (PDADMAC) and poly(styrenesulfonate) (PSS), are strong polyelectrolytes. In contrast to weak polyelectrolytes, strong polyelectrolytes fully dissociate over a wide range of solvent pH. Table 3.1 lists common properties of the both polyelectrolytes.

During the LbL process, the ionic strength of the solution determines the conformation of the adsorpt PEs. High ionic strength (> 0.5 mol/L) results in a brushy PE conformation, while low ionic strength (< 0.5 mol/L) leads to a flat conformation. The origin of the different polyelectrolyte conformations lies in the electrostatic repulsion of the charged polyelectrolyte side groups: at low ionic strength, the charged groups repel each other and the chains are largely

Table 3.1: Used strong polyelectrolytes for PEM film assembly.

Name	Molecular Formula	M_w / (kg/mol)
PSS	$-(CH_2CH(CH_2NH_2\text{HCl})^-$	70
PDADMAC	$-(C_8H_16NCl)-$	100-200

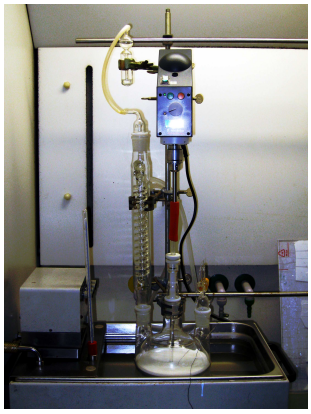

Figure 3.1: Setup for polystyrene particle synthesis.

stretched. Besides affecting its surface properties, the PE conformation determines the thickness of the PEM, which is of the order of 100 nm for a brushy, 10 nm for a flat conformation [44, 45].

3.2 Polysterene Microspheres as PEM Templates

In this thesis, latex particles serve as substrates for the PEM coating. The properties of the particles have to meet several experimental requirements, such as electrically charged surface (PE adsorption), monodispersity (rheology), and micron size (cp-afm). As an other crucial demand, a single measurement campaign requires typically about 1 kg of particles. Since the output on particles per synthesis batch is limited to about 200 g, several batches have to be mixed. Therefore, the synthesis method has to deliver particles of similar size and surface composition over all synthesis batches. To meet these demands, this thesis uses dispersion polymerization of polystyrene (PS) in ethanol [46–50]. Thereby, PS particles are made from the following recipe by using the setup depicted in Fig. 3.1

The styrene monomere (200 g), poly(vinylpyrollidone) (PVP K30, 32 g) as stabilizer, nonionic surfactant (Triton X-305, 11.2 g) as co-stabilizer, and ethanol (800 g) were weighed into a 2 l three-neck reaction flask. The filled flask was placed in a 75 °C oil heating bath and permanently stirred at 70 1/min. A starter solution with styrene monomere (40 g) and initiator 2 2'-azobis-(2-methylbutyronitrile) (AMBN, 8 g) was mixed in a beaker glass and homogenized by a magnetic stirrer at 40 °C. The reaction was initiated, when the starter solution was poured into the polymerization solution. After 24 hours, the solution was cooled down to room temperature to stop the polymerization. The particles were washed four times with ethanol by

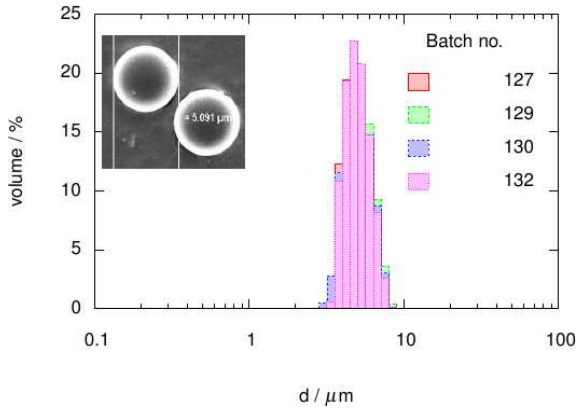

Figure 3.2: Particle size distribution of four syntheses batches with similar particle size, mean radius $a = 2.5$ µm. These batches can be safely mixed to achieve about 1 kg quasi monodisperse PS particles.

centrifugation and decanting the supernatant. Subsequently, the particles were dried and sieved (20 µm mesh size) to remove any larger aggregates.

The particle size is estimated by dynamic light scattering (DLS) and microscopy. Please have a look to Sec. 2.3.3 for a description of these methods. Throughout this thesis, particles have a mean radius $a = 2.5$ µm and a polydispersity of about 3%, as shown in Fig. 3.2.

The particles are sterically stabilized through the poly(vinylpyrollidone), which builds an about $10 - 20$ nm thick corona [51]. Zeta potential measurements revealed a surface charge of about $\zeta = -55$ mV, Fig. 3.3.

3.3 Polyelectrolyte Multilayer Modification

The polyelectrolytes were purchased from Sigma Aldrich and used without further purification. Deposition solutions were prepared dissolving monovalent salt, NaCl or KCl, in ultra pure water at the desired concentration. In this thesis, up to three different salt concentrations, 0.01, 0.5, and 1 mol/L, were used for the preparation of the deposition solution. The polyelectrolytes, PDADMAC and PSS, are added at a concentration of 0.01 mol/L.

The complete preparation takes place in centrifugal beakers. Separate centrifugal beakers were used for polyanion and polycation deposition. The PS particles were added to the deposition

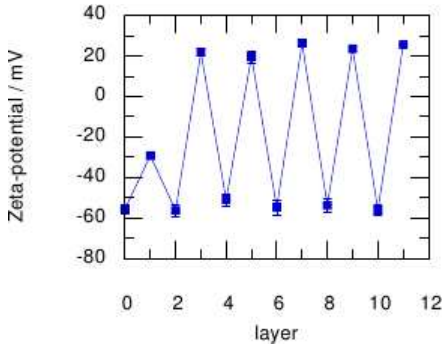

Figure 3.3: Surface charge in terms of ζ-potential versus layer number for the experimental batch depicted in Fig. 3.2.

solution under permanent stirring and immediately placed in a lab shaker. The shaker induces a shear flow within the centrifugal beakers which prevents particle agglomeration and supports polyelectrolyte adsorption [52]. After 30 min of shaking, the particles were washed by centrifugation at 3000 1/min, and subsequently decanting and replacing the supernatant by fresh electrolyte (*i.e.* deposition solution without added polyelectrolyte). The washing cycle was repeated three times prior to the subsequent adsorption step.

Adding a polyelectrolyte layer reverses the sign of the ζ-potential. The ζ-potential is about $+25$ mV for PDADMAC and -55 mV for PSS terminated samples, as seen in Fig. 3.3.

4

Yielding and Structural Relaxation in Soft Materials

4.1 Abstract

Rheological properties of soft materials are often investigated in oscillatory shear and characterized by the storage and loss modulus, G' and G'', respectively. Unfortunately, the relaxation dynamics of most soft materials is too slow to be directly probed by commercial rheometers. Recently, it was shown by Wyss *et al.* [Phys. Rev. Lett. **98**, 238303 (2007)], that the application of an oscillating strain-rate drives such soft materials and shifts the structural relaxation to higher times. They called this experimental technique strain-rate frequency superposition (SRFS). The great benefit of SRFS is the extremely extended frequency range. As viscoelastic measures, Wyss *et al.* proposed the familiar storage and loss modulus. Using these moduli results in a serious drawback: When the material yields, nonlinearities appear and the physical interpretation of the storage and loss modulus breaks down. Thus, SRFS as proposed by Wyss *et al.* is limited to the linear regime and the benefit of the extended frequency regime vanishes. In the present work, we validate an alternative data analysis technique, recently established as the stress decomposition method (SDM) [J. Rheol. **49**, 747 (2005), J. Rheol. **52**, 1427 (2008)], for the combination with SRFS. The use of SDM provides a physical interpretation of the linear and nonlinear SRFS data in terms of strain-stiffening/-softening as well as shear-thickening/-thinning.

4.2 Introduction

Especially at the yield transition, the rheology of many soft materials exhibits surprisingly universal features. The investigation of this yield behavior is hindered by the dominance of ultraslow relaxation processes [53]. Recently, Wyss *et al.* [35] proposed a method to access these ultraslow structural relaxation processes. The basic idea of their strain-rate frequency superposition (SRFS) method is to drive the soft material by the application of an constant strain-rate amplitude in oscillatory rheology. Then, the relaxation dynamics are visualized in a spectrum plot of the complex shear modulus $G^*(\omega) = G'(\omega) + \mathrm{i}G''(\omega)$ versus the angular frequency ω. The real part, the storage modulus G', represents the elastically stored energy during an oscillatory cycle, while the imaginary part, the loss modulus G'' represents the energy loss during the same cycle. Both moduli, obtained from several constant-rate sweeps with varying amplitude, can be shifted along the frequency axis to create a master curve. The master curve dramatically extends the frequency range of the relaxation spectrum in the direction to low frequencies (long relaxation times ω^{-1}).

There is an exploding interest in the SRFS method, as can be seen by its successful application to a broad variety of soft materials like suspensions [35, 54], emulsions [35, 54], foams [35], polymeric systems [55, 56], interfacial particle monolayers [57, 58] or soft tissues [59]. Unfortunately, in all cited works, the constant-rate sweeps are performed at low frequencies and large strain amplitudes – a regime in which a nonlinear stress response is expected. If so, the reported storage and loss moduli only capture the base wave $G' \to G'_1$ and $G'' \to G''_1$, and can no longer serve as a measure for the elastically stored or viscously dissipated energy [60]. Therefore, the physical meaning of the reported master curves is somewhat arbitrary. A possible way to extend SRFS to the nonlinear regime was proposed by Kalelkar *et al.* [61]. The authors of [61] used Fourier-Transform (FT) rheology [32] to decompose the nonlinear stress response to an applied sinusoidal strain by a Fourier series, with the Fourier coefficients representing the nth-order moduli G'_n and G''_n, respectively [26]. However, the higher-order moduli also have no clear physical meaning. Hence, the higher-order moduli fail to interpret the nonlinear structural relaxation in a physically meaningful sense. But such a physical interpretation is essential to explore the rheological properties of soft materials and to improve the understanding of still less-understood soft matter phenomena like yielding or shear-banding. A truly nonlinear physical interpretation of these phenomena might have an impact on basic research for the investigation of jamming or glass transition as well as for the development and improvement of constitutive models [62, 63].

The main goal of the present work is to propose such a nonlinear physical interpretation of the yield transition as well as the structural relaxation. For this, we use an alternative approach to FT rheology. The underlying principle of our alternative approach is based on the stress decomposition method (SDM), recently developed by [33, 34]. In contrast to FT rheology, the nonlinear measures obtained from SDM have a clear physical meaning like strain-stiffening/-softening or shear-thickening/-thinning.

In this work, we validate the stress decomposition method (SDM) as a tool to analyze experimental data from strain-rate frequency superposition (SRFS). We show that a stress decomposition in the deformation domain fully recovers the features obtained by the Fourier decomposition in the time domain. Further, we demonstrate that SDM gives a more detailed insight into the local viscoelastic behavior of soft materials than any other method at hand. Using the stress decomposition method, we quantify important material properties like strain-stiffening/-softening or shear-thickening/-thinning of a soft material and show their evolution with the relaxation frequency. Finally, we emphasize the importance of the strain-rate on the viscous material properties, especially when the material starts to yield.

The structure of this work is as follows. In the next section, we start with a recapitulation of the used data analysis techniques – FT rheology and SDM. This theoretical background provides the basis for the experiments which we present in section 7.4. There, we firstly prepare a rheological fingerprint of our soft material. With the help of this fingerprint, we show that SRFS recovers the characteristic features of the deformation domain. After that we compare the results from SRFS, analyzed by FT rheology with those analyzed by SDM. Finally, in the last section we sum up our results.

4.3 Theoretical Background

4.3.1 Fourier-Transform (FT) Rheology

The basic idea of FT rheology is the decomposition of the oscillating stress response $\sigma(t;\omega,\gamma_0)$ of an isotropic, viscoelastic material to a sinosoidal applied strain

$$\gamma(t) = \gamma_0 \sin(\omega t) \tag{4.1}$$

by a Fourier series according to:

$$\begin{aligned}\sigma(t;\omega,\gamma_0) =& \gamma_0 \sum_{n:odd} G'_n(\omega,\gamma_0)\sin(n\omega t) \\ &+\gamma_0 \sum_{n:odd} G''_n(\omega,\gamma_0)\cos(n\omega t)\ .\end{aligned} \tag{4.2}$$

In this decomposition, the Fourier coefficients represent the nth-order moduli G'_n and G''_n, respectively [26]. They can be calculated corresponding to:

$$\begin{aligned}G'_n(\omega,\gamma_0) &= \frac{|\sigma_n|}{\gamma_0}\cos(\delta_n) \text{ and} \\ G''_n(\omega,\gamma_0) &= \frac{|\sigma_n|}{\gamma_0}\sin(\delta_n)\ ,\end{aligned} \tag{4.3}$$

with the magnitude of the stress harmonics $|\sigma_n|$, and the phase δ_n corresponding to the applied strain. Since the stress response must be independent of the shear direction, only odd terms contribute to the Fourier series. The occurence of even terms in experimental data can be due to boundary effects, like wall slip [64, 65] or edge fracture [66], or flow inhomogeneities such as secondary flows [67].

Based on the constitutive model of a nonlinear viscoelastic material developed by Green and Rivlin [68], Ganeriwala and Rotz [69] showed that the dissipated energy per volume during a full oscillation cycle $E_d(t;\omega,\gamma_0) = \int_0^{2\pi/\omega} \sigma \mathrm{d}\gamma$ is solely a function of the loss modulus, $E_d = \pi\gamma_0^2 G_1''$, and hence:

$$G_1'' \propto E_d \; . \tag{4.4}$$

This relation was recently experimentally verified for several soft materials by Kalelkar *et al.* [61]. Hence, it is plausible that all occurring higher-order moduli, G_n' and $G_{n>1}''$, have to contribute to a reversible stored energy. As a measure for the stored energy, we propose a generalized modulus

$$\tilde{G}' = \sum_{1}^{n:odd} G_n' + \sum_{3}^{n:odd} G_n'' \; . \tag{4.5}$$

4.3.2 Stress Decomposition Method (SDM)

Because of the time-dependence of the applied strain $\gamma(t)$ after equation (4.1), the samples also experience a strain-rate

$$\dot{\gamma}(t) = \dot{\gamma}_0 \cos(\omega t) \; , \tag{4.6}$$

with the strain-rate amplitude $\dot{\gamma}_0 = \gamma_0\omega$. Then it is obvious to decompose the resulting stress $\sigma(t;\gamma,\dot{\gamma})$ in an elastic stress $\sigma'(t;\gamma)$ in phase with the strain, and a viscous stress $\sigma''(t;\dot{\gamma})$ in phase with the strain-rate [33, 70]:

$$\sigma(t;\gamma,\dot{\gamma}) = \sigma'(x) + \sigma''(y) \; , \tag{4.7}$$

with $x = \gamma(t)/\gamma_0 = \sin(\omega t)$ and $y = \dot{\gamma}(t)/\dot{\gamma}_0 = \cos(\omega t)$ designating the normalized strain and strain-rate, respectively. The single-valued functions of the elastic and viscous stress, respectively, can be approximated using Chebyshev series [34]:

$$\begin{aligned} \sigma'(x) &= \gamma_0 \sum_{n:odd} e_n(\omega,\gamma_0) T_n(x) \; , \\ \sigma''(y) &= \dot{\gamma}_0 \sum_{n:odd} v_n(\omega,\gamma_0) T_n(y) \; . \end{aligned} \tag{4.8}$$

Here T_n is the nth-order Chebyshev polynomial of the first kind, and e_n and v_n are the elastic and viscous Chebyshev coefficients, respectively. The choice of Chebyshev polynomials of the first kind was motivated by Ewoldt *et al.* [34] due to the following reasons: they (i) are bounded, (ii) exhibit odd symmetry about $x = 0$ and (iii) form an orthogonal basis over the finite integration domain [-1,+1] (because $-1 \leq x,\, y \leq +1$).

A physically meaningful interpretation of the higher-harmonic stress contributions was given by Ewoldt *et al.* [34] through the elastic and viscous Chebyshev coefficients: any positive contribution of, for example, the third-order Chebyshev polynomial $T_3(x) = 4x^3 - 3x$ [71] must result in a higher elastic stress at the maximum dimensionless strain at $x \to 1$, than the elastic stress contribution represented by the first-order Chebyshev polynomial $T_1(x) = x$ alone. Ewoldt *et al.* argued that the third order is the leading order and introduced the elastic and viscous Chebyshev intensities e_3/e_1 and v_3/v_1, respectively. While the first-order Chebyshev polynomials are always positive, e_3/e_1 indicates strain-stiffening when it has a positive sign, whereas a negative e_3/e_1 indicates strain-softening. Analogously, a positive v_3/v_1 indicates shear-thickening, while a negative v_3/v_1 indicates shear-thinning.

Nevertheless, there may exist soft materials, where it is not sufficient to take only the third order contribution into account [72]. To allow for significantly higher-harmonic contributions, we introduce the higher-order elastic and viscous Chebyshev intensities

$$\begin{aligned} E &= \sum_{3}^{n:odd} e_n/e_1 \ , \\ V &= \sum_{3}^{n:odd} v_n/v_1 \ , \end{aligned} \tag{4.9}$$

respectively. In equation (4.9), the individual terms e_n/e_1, v_n/v_1 may have a negative or positive sign. Hence, E and V indicate the overall shear-thinning/-thickening behavior of the material.

The viscoelastic moduli $\tilde{G}'$ and G_1'', as defined in section 4.3.1, and the higher-order Chebyshev intensities E and V quantify the average stress response over a full oscillation cycle. To investigate the viscoelastic behavior within an oscillation cycle, Ewoldt *et al.* [34] introduced the differential measures *minimum-strain modulus* and the *minimum-rate dynamic viscosity*,

$$\begin{aligned} G'_M &= \left.\frac{\mathrm{d}\sigma}{\mathrm{d}\gamma}\right|_{\gamma=0} \\ &= \sum_{n:odd} nG'_n = e_1 - 3e_3 + \dots \ , \\ \eta'_M &= \left.\frac{\mathrm{d}\sigma}{\mathrm{d}\dot{\gamma}}\right|_{\dot{\gamma}=0} \\ &= \frac{1}{\omega} \sum_{n:odd} (-1)^{(n-1)/2} nG''_n = v_1 - 3v_3 + \dots \ , \end{aligned} \tag{4.10}$$

respectively, which describe the viscoelastic properties at zero instantaneous strain and strain-rate; and in a similar fashion, the *large-strain modulus* and the *large-rate dynamic viscosity*,

$$\begin{aligned} G'_L &= \left.\frac{\sigma}{\gamma}\right|_{\gamma=\pm\gamma_0} \\ &= \sum_{n:odd} (-1)^{(n-1)/2} G'_n = e_1 + e_3 + \dots , \\ \eta'_L &= \left.\frac{\sigma}{\dot{\gamma}}\right|_{\dot{\gamma}=\pm\dot{\gamma}_0} \\ &= \frac{1}{\omega} \sum_{n:odd} G''_n = v_1 + v_3 + \dots , \end{aligned} \tag{4.11}$$

respectively, which characterize the viscoelastic behavior at maximum instantaneous strain and strain-rate.

It is important to note that the differential measures, equations (4.10) and (4.11), can be obtained via two different methods; geometrically from Lissajou figures, or by stress decompostition using FT rheology or SDM. Following the SDM approach to estimate G'_L and η'_L as shown by equation (4.11), the higher-order elastic and viscous Chebyshev intensities, equation (4.9), may be interpreted as a reduced large-strain modulus $E = G'_L/e_1$-1 and a reduced large-rate dynamic viscosity $V = \eta'_L/v_1$-1.

4.4 Experiments

4.4.1 Rheological Fingerprint of a Model Polymer Gel

We used a strain controlled rheometer (ARES G2, TA Instruments) to apply a sinosoidal strain according to equation (4.1) to the samples. We performed all measurements at 20 °C in a cone-plate geometry (diameter 40 mm, cone angle 0.02 rad and gap truncation 0.027 mm) equipped with a rough plate and a solvent trap to prevent wall slip and evaporation, respectively. For data analysis, we recorded the data of 5 full cycles after waiting 10 full cycles for the sample to reach a steady state. We interpolated the data, with a resolution of 5 data points in the strain direction and 2 data points in the frequency direction.

As an experimental example, we report on the material properties of a commercial hair gel (WetGel, REWE, Germany). This material exhibits dominant elasticity ($e_3/e_1 \approx 0$) up to strains of about $\gamma_0 = 20\%$ as seen in figure 4.1(a). For larger applied strains, the gel stiffens, quantified by a rising elastic intensity. The viscous Chebyshev intensity v_3/v_1 is visualized in

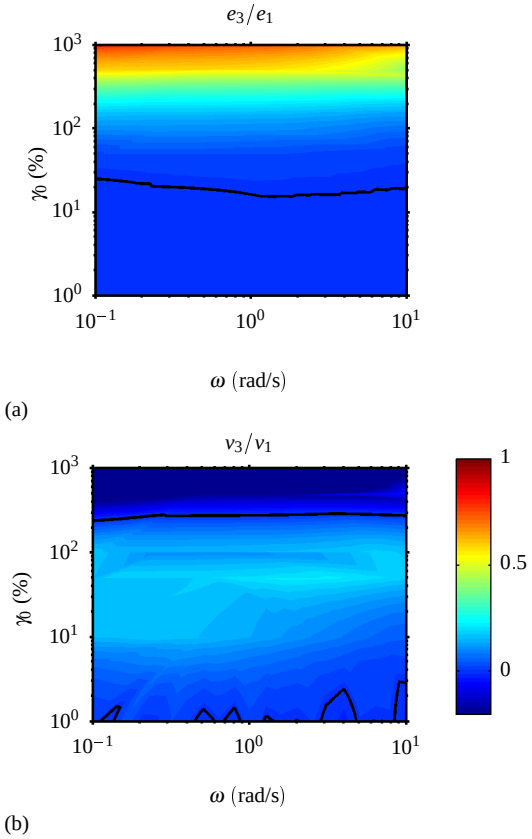

Figure 4.1: Rheological fingerprint of (a) elastic, e_3/e_1, and (b) viscous, v_3/v_1 Chebyshev intensities versus the frequency ω. As an indicator for the strain-stiffening/-softening and the shear-thickening/-thinning transition, the zero isolines are marked by a black solid line.

figure 4.1(b). This figure identifies a positive maximum at medium strains, revealing shear-thickening. At larger strains ($\gamma_0 > 200\%$), the sign of v_3/v_1 changes and the material behavior switches to shear-thinning. Both the elastic and viscous Chebyshev intensities are independent of the angular frequency ω in the domain shown in figure 4.1.

The viscoelastic fingerprint in terms of the elastic and viscous Chebyshev coefficients extends the range to the nonlinear domain, in which a physically meaningful interpretation of the rheological behavior is possible. But it is also obvious from figure 4.1, that such a fingerprint can not give any information on the relaxation dynamics, since the measures are independent of the frequency over the entire experimental range.

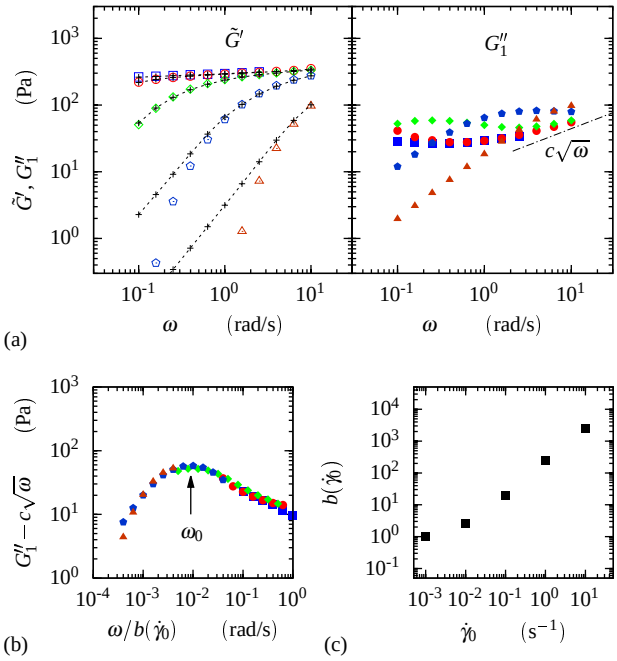

Figure 4.2: (a) The generalized $\tilde{G}'$ and the loss modulus G_1'' of the constant-rate tests plotted against the frequency. The strain-rate amplitudes are 10^{-3} (squares), 10^{-2} (circles), 10^{-1} (diamonds), 10^{0} (pentagons) and 10^{1} (triangles) rad/s. The points with connected lines show the first order elastic modulus G_1'. In the high frequency limit, several G_1'' curves rise proportional to $c\sqrt{\omega}$ (chain line). (b) Isolation of the relaxation peak. (c) The corresponding shift factor $b(\dot{\gamma}_0)$ versus the strain-rate amplitude $\dot{\gamma}_0$.

4.4.2 Application of Strain-Rate Frequency Superposition (SRFS) to the Polymer Gel

We scanned the deformation space of the rheological fingerprint (figure 4.1) with several constant-rate sweeps and analyzed the data first by FT rheology and then by SDM to compare the performance of both methods.

By means of FT rheology, we briefly introduce the SRFS procedure of Wyss *et al.* [35]. Raw unshifted curves of the viscoelastic moduli are plotted in figure 4.2(a). We determine the strain-rate independent elastic plateau modulus $\tilde{G}'|_{\dot{\gamma}_0 \to 0} = \tilde{G}_0'$ (squares) and the strain-rate independent relaxation frequency $\omega(\dot{\gamma}_0)|_{\dot{\gamma}_0 \to 0} = \omega_0$ as references for the shifts, respectively along the amplitude and the frequency axis. Unfortunately, ω_0 is masked by the increasing G_1'' with increasing frequencies. This high frequency response is proportional to $\sqrt{\omega}$ (chain line), which

allows to isolate the relaxation frequency. For this, we subtract the high frequency response $c\sqrt{\omega}$, c is a proportionality factor, from the raw G_1''-data and shift them along the frequency axis. This procedure results in a relaxation peak with a magnitude and shape that is independent of strain-rate, as seen in figure 4.2(b). Figure 4.2(c) shows the frequency shift factor $b(\dot{\gamma}_0)$ as a function of the strain-rate amplitude $\dot{\gamma}_0$. Hence, the shift factors are defined as: $a_G(\dot{\gamma}_0) = \tilde{G}'(\dot{\gamma}_0)/\tilde{G}'_0$, $b(\dot{\gamma}_0) = \omega(\dot{\gamma}_0)/\omega_0$.

4.5 Evaluation of the Experimental SRFS Data

4.5.1 Results from Fourier-Transform (FT) Rheology: Phenomenological (Qualitative) Description of Structural Relaxation

First, we quantify the nonlinearity of the constant-rate sweep data. Therefore, we plot in figure 4.3(a) the relative intensities of the nth-order stress contributions $I_n/I_1 = |\sigma_n|/|\sigma_1|$.

As expected, higher harmonic moduli appear with decreasing frequency and increasing strain-rate amplitude. This observation helps us to identify in figure 4.3(a) three regimes: (i) in small amplitude oscillatory shear (SAOS), $\omega/b(\dot{\gamma}_0) > 2\times10^{-1}$ rad/s, only the first-order moduli contribute to the stress response, while (ii) moderate higher harmonic contributions appear as the material yields (frequencies between 3×10^{-4} and 2×10^{-1} rad/s), whereas in (iii) large amplitude oscillatory shear (LAOS), I_n/I_1 plateaus at 5% (I_9/I_1) to 20% (I_3/I_1). Note, *amplitude* in the phrases "small amplitude oscillatory shear" (SAOS) and "large amplitude oscillatory shear" (LAOS) refers to both, strain amplitude γ_0 and strain-rate amplitude $\dot{\gamma}_0$.

The shapes of the generalized $\tilde{G}'$ and first order G_1'' moduli given in figure 4.3(b) show the typical features of a soft material with a frequency independent $\tilde{G}' > G_1''$ at high frequencies. With decreasing frequencies, $\tilde{G}'$ decreases as well, while G_1'' first passes through a maximum at the relaxation frequency $\omega_0/b(\dot{\gamma}_0) = \omega_0$. Then, it subsequently decreases as a power law $G_1'' \propto \omega^{-\nu''}$ with $\nu'' = 1$. The generalized modulus $\tilde{G}'$ diverges at a reduced frequency of about 3×10^{-4} rad/s. For comparison with other works and validation of our experiments, we also plot in figure 4.3(b) the first-order storage modulus G_1' (connected points) and recognize that it decreases also as a power-law $G_1' \propto \omega^{-\nu''}$ with $\nu' = 1.7$. This is in reasonable good agreement with a Maxwell model in linear viscoelasticity, which predicts the relation $\nu' = 2\nu''$ [62, 73], as well as experimental data reported in [35, 54–59].

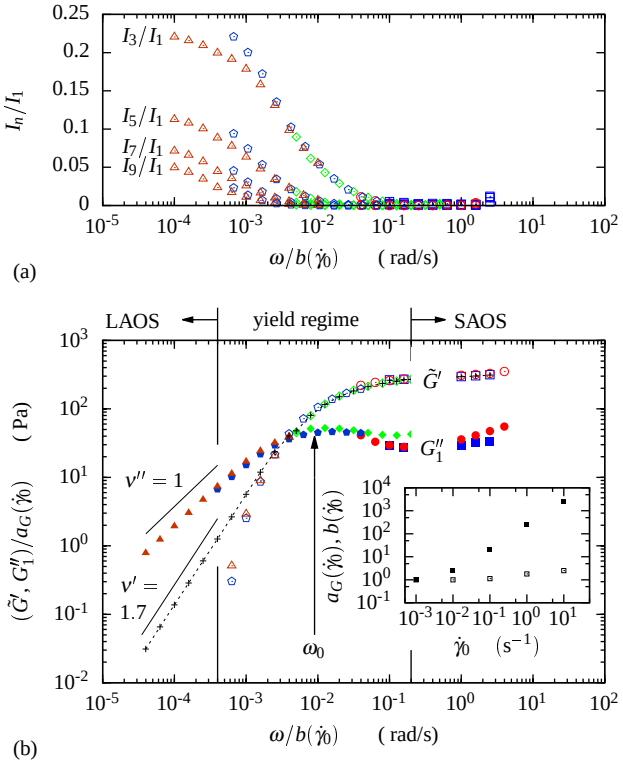

Figure 4.3: Relaxation spectrum obtained by FT rheology for several constant-rate sweeps. (a) Non-linearity expressed through the intensity ratios I_n/I_1. (b) Master curves of $\tilde{G}'$, G_1'' and, for comparison, G_1' (connected points). Each color represents data from a single constant-rate sweep. The inset shows the shift factors $a_G(\dot{\gamma}_0)$ (open) and $b(\dot{\gamma}_0)$ (solid) as functions of the corresponding strain-rate amplitudes.

4.5.2 Results from Stress Decomposition Method (SDM): Physical (Quantitative) Description of Structural Relaxation

In this section, we reinterpret the FT rheology data in the framework of the SDM with the physical meaning of the higher-order elastic and viscous Chebyshev intensities, E and V, respectively, after equation (4.9).

According to figure 4.3(b), we plot in figure 4.4 the master curves of the higher-order elastic and viscous Chebyshev intensities, E and V, respectively, as a function of the reduced frequency. Surprisingly, the E and V curves shift with the same $b(\dot{\gamma}_0)$ as previously demonstrated by the $\tilde{G}'$ and G_1'' curves.

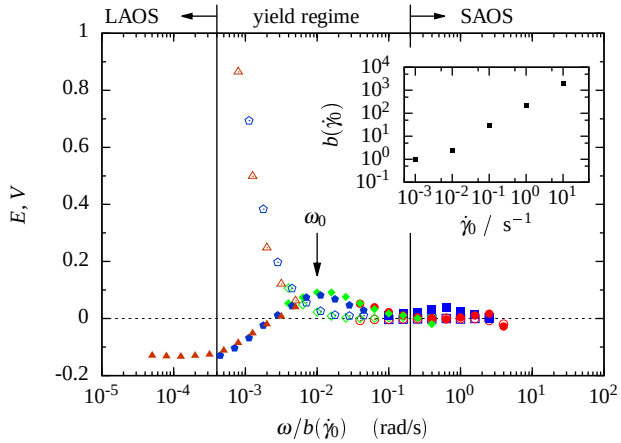

Figure 4.4: Relaxation spectrum in terms of SDM. Master curve of E (open) and V (solid); inset: shift factor $b(\dot{\gamma}_0)$ as a function of the strain-rate amplitude. Each color represents data from a single constant-rate sweep.

In figure 4.4, the zero E and V values indicate the linear SAOS regime.

In the yield regime, V starts to increase, revealing a shear-thickening stress contribution, while the elastic stress contribution remains linear ($E \approx 0$). The increase in V in figure 4.4 coincides with the increase of G_1'' in figure 4.3(b), respectively linking the shear-thickening with the increasing energy dissipation during yielding. The shear-thickening reaches its maximum at the relaxation frequency ω_0.

From this observation follows, that there is a universal relaxation mechanism that is independently detected by FT rheology and SDM. This is also expressed through the existence of a single frequency shift factor $b(\dot{\gamma}_0) = \omega(\dot{\gamma}_0)/\omega_0$ for all experiments.

The shear-thickening peak is accompanied by the onset of strain-stiffening ($E > 0$). In the following sections, we will discuss the relation of this yield transition to the structural relaxation in more detail.

The nonlinear LAOS regime is characterized by two features, a shear-thinning contribution with a constant value V of about -0.125 and a diverging strain-stiffening at a frequency $\omega/b(\dot{\gamma}_0)$ $\approx 4 \times 10^{-4}$ rad/s which is similar to the abrupt decrease of $\tilde{G}'$ in figure 4.3(b), indicating the dramatic loss in the ability to reversibly store energy.

The fact that the first-order modulus G_1'' dominates the nonlinear behavior of the viscous measure V, verifies the assumption that in FT rheology the higher-order moduli, G_n' and $G_{n>1}''$,

contribute to the reversibly stored energy after equation (4.5) and hence our proposed generalized modulus $\tilde{G}'$ serves as an appropriate nonlinear viscoelastic measure in FT rheology.

4.5.3 Cycle Averaged Viscosity

The sample shows the typical behavior of a shear-thinning pseudoplastic material. A more familiar representation of shear-thinning as a plot of G_1'' gives the dynamic viscosity $\eta_1' = G_1''/\omega$. The η_1' curves are shifted along the frequency axis by the use of the same shift factors $b(\dot{\gamma}_0)$ as previously for G_1''. In LAOS, G_1'' is proportional to ω^{-1} and the dynamic viscosity plateaus at the zero-rate viscosity, $\eta_1'(\dot{\gamma}_0)|_{\dot{\gamma}_0 \to 0} = \eta_0'$. Hence, the amplitude shift factor is defined as $a_\eta(\dot{\gamma}_0) = \eta_1'(\dot{\gamma}_0)/\eta_0'$.

The η_1'-master curve in figure 4.5(a) follows a power-law

$$(\eta_1' - c/\sqrt{\omega})/a(\dot{\gamma}_0) = \eta_0'(1 + (\lambda'\omega/b(\dot{\gamma}_0))^2)^{(n'-1)/2} \ , \tag{4.12}$$

with the parameters η_0', λ' and n'. Subtracting $c\sqrt{\omega}$ aligns the tails of the high frequency response (connected points) at the power law. This power-law is reminiscent of a Carreau fluid

$$\eta(\dot{\gamma}) = \eta_0(1 + (\lambda\dot{\gamma})^2)^{(n-1)/2} \ , \tag{4.13}$$

often used to describe pseudoplasticity. Herein is λ a time constant for the onset of shear-thinning and the exponent n the slope in the shear-thinning region. Steady shear experiments, which we do not show here, provide the parameters of the Carreau fluid. Directly comparing equation (4.12) with equation (4.13) reveals $\eta_0' \approx \eta_0$ and $\lambda' \approx \lambda$. Hence, the dynamic and the steady shear viscosity are equal, $\eta_1'(\dot{\gamma}_0)|_{\dot{\gamma}_0 \to 0} \approx \eta(\dot{\gamma})|_{\dot{\gamma} \to 0}$.

In contrast to the viscoelastic moduli, the amplitude shift factor $a_\eta(\dot{\gamma}_0)$ changes over several decades, as seen in figure 4.5(b). Also, $a_\eta(\dot{\gamma}_0)$ is now a linear function of $b(\dot{\gamma}_0)$, figure 4.5(c), which represents a shift along the viscosity of the background fluid. Similar behavior is observed for viscoelastic gels in frequency sweep experiments [74, 75].

4.5.4 Local Viscoelasticity

Now, we turn our attention to the differential measures, i.e. the minimum- and large-strain modulus (G_M', G_L') as well as the minimum- and large-rate dynamic viscosity (η_L', η_M'), defined by equations (4.10) and (4.11). As discussed in section 4.3.2 and in contrast to the integral measures reported before, these measures allow us to peek into the oscillation cycle, reflecting the instantaneous loading/unloading of the material. First, we assure that the curves of the

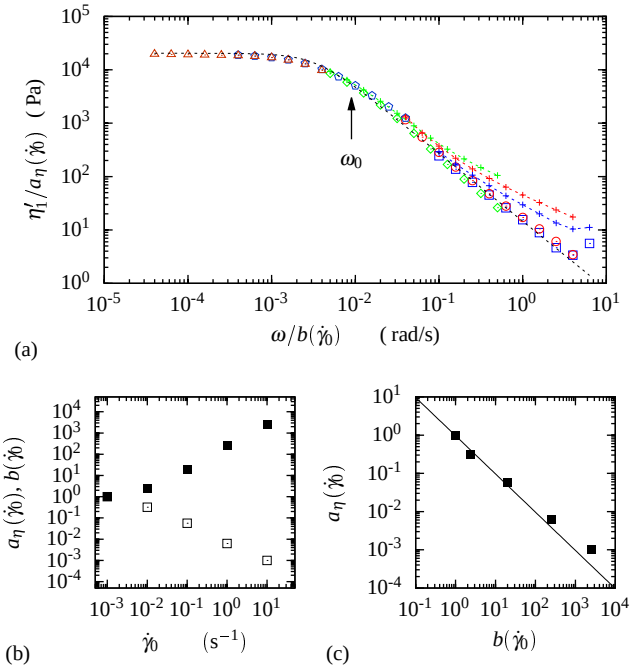

Figure 4.5: (a) First-order dynamic viscosity η_1' as function of the reduced frequency $\omega/b(\dot\gamma_0)$. The dashed curve is a fit to the power-law equation (4.12). Viscosity data for $\omega > \omega_0$ are high frequency corrected; uncorrected data are marked by the connected points. (b) Shift factors $a_\eta(\dot\gamma_0)$ (open) and $b(\dot\gamma_0)$ (solid) as functions of the strain-rate amplitude. (c) Amplitude shift factor $a_\eta(\dot\gamma_0)$ as a function of the frequency shift factor $b(\dot\gamma_0)$. Each color represents data from a single constant-rate sweep.

minimum- and large-strain modulus (G_M', G_L') as well as the minimum- and large-rate dynamic viscosity (η_L', η_M') can be superimposed onto the master curves in figure 4.6, using the same procedure as before. Figure 4.7 shows the corresponding shift factors $a_\eta(\dot\gamma_0)$ and $b(\dot\gamma_0)$.

In the linear SAOS regime, the curves of G_M' (η_M') and G_L' (η_L') are identical as can be seen in figure 4.6(a), (b). With rising nonlinearity, these curves split into separate curves for G_M' (η_M') and G_L' (η_L'). When the curves separate, the ratio $G_L'/G_M' > 1$ indicates strain-stiffening and $\eta_L'/\eta_M' < 1$ marks shear-thinning.

Remarkably, in the LAOS regime, a secondary, low frequency plateau in G_M' arises (arrow in figure 4.6(a)) which could not be detected with any of the other measures.

The separation of the local measures in the yield regime is likely due to a competition between the rate of bond-breaking and the rate of bond-recovery [76, 77]. Then, the experi-

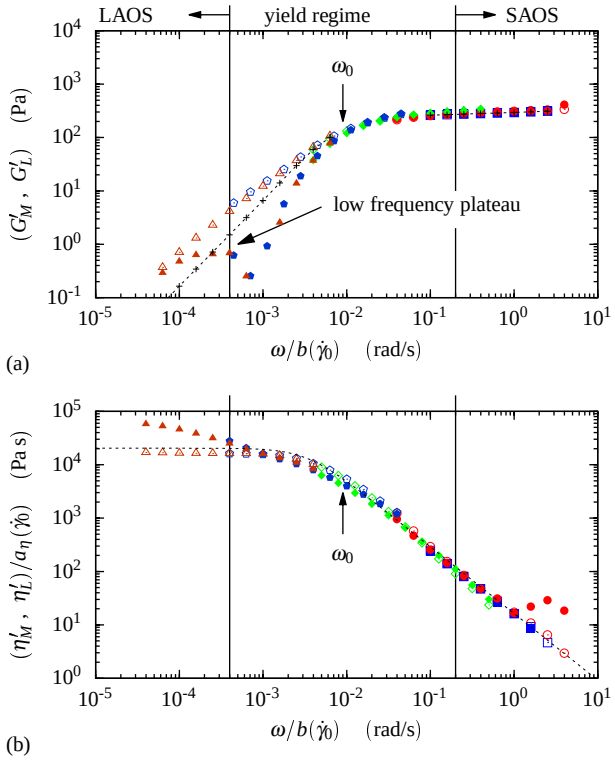

Figure 4.6: The local viscoelastic measures as functions of the reduced frequency $\omega/b(\dot\gamma_0)$. (a) presents the elastic moduli G'_M (solid) and G'_L (open). For the sake of comparison, G'_1 is also shown (connected points). (b) illustrates the corresponding viscosities η'_M (solid) and η'_L (open) as well as the power-law fit to equation (4.12) (dashed line). Each color represents data from a single constant-rate sweep.

mental frequency $\omega(\dot\gamma_0)$ and the internal relaxation frequency $\omega_i(\dot\gamma_0)$ are of the same order $\omega(\dot\gamma_0)/\omega_i(\dot\gamma_0) \approx 1$. This behavior is quite universal for soft materials [35, 62]. The structural relaxation of such a material is given by the phenomenological expression [62]

$$\omega_i(\dot\gamma_0) = \omega_0 + K|\dot\gamma_0|^\nu \ . \tag{4.14}$$

In this equation ω_0 denotes the relaxation frequency as defined before, K is a fit parameter and ν describes the behavior at high strain-rates. A plot of equation (4.14) as a fit to the frequency shift factor $b(\dot\gamma_0)$, obtained from figures 4.3(b) and 4.4, is depicted in figure 4.7. The estimated exponent $\nu = 1$ is in perfect agreement with that given by [35, 62]. Hence, equation (4.14) can be used to reconstruct the structural relaxation frequency $\omega_i(\dot\gamma_0)$ from the master curves.

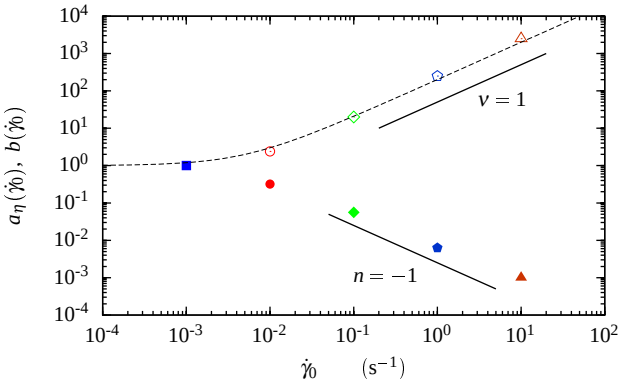

Figure 4.7: Evolution of the amplitude shift factor $a_\eta(\dot\gamma_0)$ (solid) and the frequency shift factor $b(\dot\gamma_0)$ (open) as functions of the strain-rate. The structural relaxation frequency $\omega_i(\dot\gamma_0)$, obtained by fitting equation (4.14) to $b(\dot\gamma_0)$, is drawn as the dashed line. Each color represents data from a single constant-rate sweep. The symbols at $\dot\gamma_0 = 10^{-3}$ s^{-1} collapse.

4.5.5 Local Viscoelasticity by Lissajous - Bowditch Figures

Lissajous-Bowditch figures give a qualitative representation of the local viscoelastic behavior. We refer to elastic Lissajous-Bowditch figures as stress $\sigma(t)$ versus strain $\gamma(t)$, viscous Lissajou-Bowditch figures as stress $\sigma(t)$ versus strain-rate $\dot\gamma(t)$ plots of a single, steady oscillation cycle. The Lissajou-Bowditch curves in figure 4.8(a) visualize the linear viscoelastic stress response of the sample in the SAOS regime. In the yield and LAOS regime, the shapes of the Lissajous-Bowditch curves change significantly, as observed by figure 4.8(b). With increasing strain amplitude, the elastic Lissajous-Bowditch curves increasingly equal a rectangle. The corresponding viscous Lissajous-Bowditch figures reveal a dominant viscous behavior. This is also demonstrated by the traces of the viscous stress $\sigma''(t)$, which closely approximates the loops of the total stress $\sigma(t)$. At the same time, the elastic stress $\sigma'(t)$ vanishes. These results support the observations of the diverging $\tilde{G}'$ (figure 4.3(b)) and E (figure 4.4) in LAOS.

To quantify such plastic behavior, Ewoldt *et al.* [78] proposed the plastic dissipation ratio $\phi = E_d/E_{d,pp}$. This measure relates the dissipated energy E_d to the dissipated energy of a perfect plastic material $E_{d,pp} = (2\gamma_0)(2\sigma_{max})$. We have to note, that shifting the plastic dissipation ratio ϕ with $b(\dot\gamma_0)$ along the frequency axis also creates a master curve similar to those discussed before.

Another feature may also be explained by the Lissajous-Bowditch curves. In figure 4.6(a), the minimum-strain modulus G'_M exhibits a singular dip at $\omega/b(\dot\gamma_0) \approx 7 \times 10^{-4}$ rad/s. A possible cause for the dip may be a sign change of G'_M due to the occurence of stress overshoots [79].

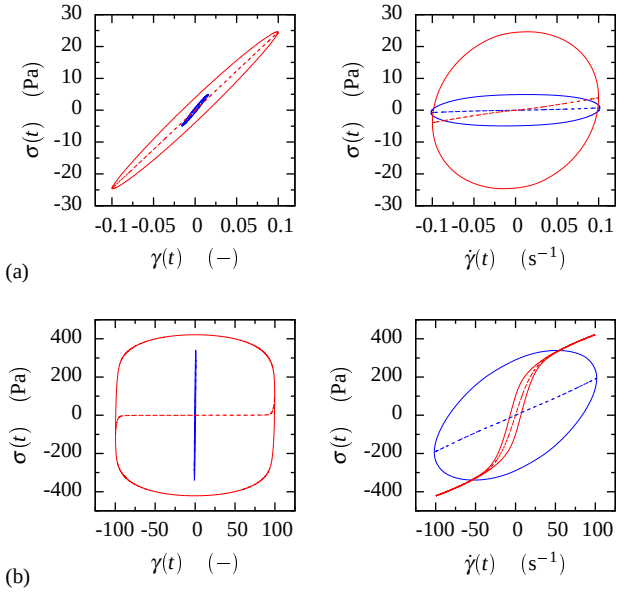

Figure 4.8: Elastic (left) and viscous (right) Lissajous-Bowditch figures for the limiting cases of a constant-rate sweep: {lowest strain, highest frequency} (blue) and {highest strain, lowest frequency} (red). (a) shows figures of the SAOS regime ($\dot{\gamma}_0 = 0.01\,\mathrm{s}^{-1}$), (b) of the LAOS regime ($\dot{\gamma}_0 = 100\,\mathrm{s}^{-1}$). The closed loops (solid lines) visualize the total stress $\sigma(t)$, whereas the elastic (viscous) stress $\sigma'(t)$ ($\sigma''(t)$) gives the single valued functions (dashed lines).

Stress overshoots are related to structural changes of the microstructure. The changes have to be (partially) reversible at time scales of the oscillatory loading. In LAOS, such stress overshoots are visualized by secondary loops in the *viscous* Lissajous-Bowditch figures. Even at the high strain-rate amplitudes of figure 4.8(b), we do not observe sign changes in G'_M or secondary loops. Hence, the changes of the microstructure are irreversible, which confirms our previous results.

4.6 Conclusions

In this work, we explored the linear and nonlinear behavior of shear driven soft materials by strain-rate frequency superposition (SRFS). We used the stress decomposition method (SDM) as an alternative approach to the classical Fourier-transform (FT) rheology to reinterpret viscoelasticity of driven soft materials. By comparing the FT rheology data with SDM data, we have demonstrated that the higher-harmonic moduli G'_n and $G''_{n>1}$, may significantly contribute

to a reversibly stored energy, quantified by the proposed generalized modulus $\tilde{G}'$. We have validated that SDM captures the relevant features of driven soft materials and, moreover, the physical meaning of the resulting data is not restricted to the linear regime alone. This also includes the local viscoelastic measures, introduced by Ewoldt *et al.* [34]. All these measures could be superimposed onto master curves by shifting the individual constant-rate sweep curves along the frequency axis. It is important to note that we used the same frequency shift factors for all measures. This fact supports the assumption of a universal relaxation behavior of soft materials. Moreover, using SRFS extends the frequency range, and thus the relaxation spectra, of the nonlinear viscoelastic measures obtained from SDM to more than 5 decades.

Thus, our results show that the combination of SRFS with SDM is a very powerful tool to gain a more detailed physical understanding of the yielding and the structural relaxation of soft materials.

5

Systematic Modification of the Rheological Properties of Colloidal Suspensions with Polyelectrolyte Multilayers

5.1 Abstract

Tailoring rheological properties of colloidal suspensions with the adsorption of polyelectrolyte multilayers (PEMs) is based on the idea of controling macroscopic mechanical properties by modifying the particle surface in a reproducible and well-understood manner. With Layer-by-Layer (LBL) self-assembly monodisperse polystyrene particles are coated with up to ten layers of the oppositely charged strong polyelectrolytes: poly(diallyl dimethyl ammonium chloride) PDADMAC and poly(styrene sulfonate) PSS. The conformation of the adsorbed polyelectrolyte is controlled by the ionic strength of the used aqueous polyelectrolyte solution. For 1M NaCl solution a brush like adsorbtion of the polyelectrolyte is expected. The ability of PEMs to serve on a nanoscale level as surface modifiers and influence macroscopic rheological properties like viscoelasticity, yield stress and shear banding is discussed. The mechanical behavior of these suspensions is qualitatively described by the theory of Derjaguin-Landau-Verwey-Overbeek (DLVO) with short-range repulsion and long-range attraction. A scaling rule is proposed which distinguishes between the precusor and the multilayer regime.

5.2 Introduction

Tailoring properties of colloids on a nanoscale level with self-assembled polyelectrolyte multilayers (PEM) via a Layer-by-Layer (LBL) coating process was introduced in the 1990s by Gero Decher and co-workers [4, 80]. The idea of nanoengineering particle surfaces and to use the modified colloids as building blocks for the creation of ordered and complex materials attracted a lot of attention during the last years [81]. This concept can be also applied to colloidal suspensions by modifying surfaces of colloidal particles on a nanoscopic level to control their macroscopic rheological properties [21, 37]. Predicting and controling rheology of colloidal suspensions matters in basic research to understand the relation between microstructure and macro behavior in condensed matter and in industrial domains to increase the efficiency of production and the product quality [18, 82].

The macroscopic behavior of suspensions is dependent on a large number of parameters due to their multiphase material character. The continuous phase, the dispersed phase and the interaction between both phases are contributing to the mechanical properties [7]. The crucial parameters to control the rheological properties of colloidal suspensions can be reduced to the particle radius a, the volume fraction ϕ and the interaction energy U between the particles [18]. In many processes the radius and the volume fraction are constant and then the interaction forces remain as single control parameter. Much work has been dedicated to interaction forces between colloidal particles [38, 83]. Attractive and repulsive forces between colloids are triggered by adjusting pH, ionic strength or adding macromolecules to the dispersion medium [37], or by direct surface modification of the colloidal particles [84]. In recent studies colloids were modified through adsorption of lipids [85], proteins [86], surfactants [87] or polymers [88, 89] onto the particle surface. Chemical functionalization was done via grafted polymer chains [84] or with the help of silanization of colloids [90]. All these experiments showed significant relations between the surface modification and the effect on the yield stress and the elasticity of suspensions.

In this work we demonstrate that PEM modification significantly alters the rheological properties of colloidal suspensions. The main advantages of LBL self-assembly are its versatile approach for a controlled surface modification which is well understood on a microscopic level, its universal application to all kind of charged particles and its high reproducibility and adjustment of the layer thickness. Here, we adjusted the ionic strength of the PE solution to 1 mol/l NaCl, this results in a coiled conformation of polyelectrolytes in solution [91] and a brush like adsorption onto the particle surface [92, 93]. We adsorped up to 10 layers on 5 µm polystyrene (PS) particles with the thickness of one PE layer in the order of 1 to 2 nm [81]. Therefore, the increase of the hydrodynamic radius by the deposited layers is negligible. Another benefit of PEM coated particles in suspensions is that the chemical composition of the dispersion medium is not altered due to the high PEM stability.

We show for the first time the influence of adsorbed PEs on elasticity, yield stress and flow

properties of the suspensions. Recent works characterizing the microstructure of PEM coatings distinguish between a multilayer regime and a precursor regime [94]. In our rheological experiments, we observed an influence of these two regimes on the elasticity and the yield stress. We show that the multilayer regime can described by the Derjaguin-Landau-Verwey-Overbeek (DLVO) theory, whereas in the precursor regime DLVO theory breaks down. Suspensions in the multilayer regime exhibit the same features as attractive, electrosterically stabilized colloidal suspensions. We validate our rheological measurements by topography images of the particle surfaces obtained by atomic force microscopy (AFM).

5.3 Materials and Methods

5.3.1 Sample Preparation

Polystyrene (PS) particles with the radius $a = 2.5$ µm are produced by a dispersion polymerization technique, details are given in Sec. 3.2, to achieve a narrow size distribution with a polydispersity of $\approx 3\%$ [46, 49].

For Layer-by-Layer (LBL) deposition, positively charged poly(diallyl dimethyl ammonium chloride) (PDADMAC, M_w =100,000-200,000 g/mol) and negatively charged poly(styrene sulfonate) (PSS, M_w =70,000 g/mol) from Sigma Aldrich (Germany) are used without further purification. PEMs are formed by layer-by-layer adsorption from 1 mol/l NaCl aqueous solution. The success of the multilayer-formation is checked by ζ-potential measurements; bare particles and PSS terminated PEMs yield a ζ-potential of -55 mV and PDADMAC terminated PEMs yield a zetapotential of $+25$ mV.

After each adsorbtion step, we seperate a certain amount of PEM coated particles and mill the separated particles at volume fractions of $\phi = 0.55$ into glycerol electrolyte (ionic strength: 10^{-2} mol/l NaCl).

5.3.2 Rheometrical Setup and Measurement Protocol

We investigate the flow and material properties of the suspensions by logarithmic ramp tests. The sample history is erased by 180 s oscillatory pre-shear (strain amplitude $\gamma_0 = 5$ and frequency $f = 1$ Hz) followed by 180 s stress relaxation at $\sigma = 0$ Pa. To take transient effects into account, we apply ramps of the form

$$f(t) = f_0 \, (f_\infty / f_0)^{t/\tau_r} \ , \tag{5.1}$$

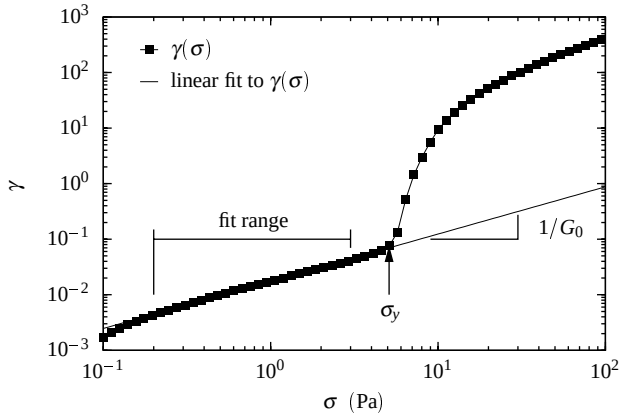

Figure 5.1: Procedure for static yield stress estimation: strain γ as a function of applied shear stress. The solid line represents the linear stress-strain regime with the slope $1/G_0$. The yield stress σ_y is indicated by an arrow.

with a constant ramp time $\tau_r = 30$ min [25]. In Eqn. (5.1), f represents $\dot{\gamma}$ in strain rate tests and σ in stress tests. The initial values are denoted by f_0, the final values by f_∞. In stress controlled experiments, the initial and final stress values are determined from the strain rate tests ($\sigma_0 = \sigma|_{\dot{\gamma}_0}$ and $\sigma_\infty = \sigma|_{\dot{\gamma}_\infty}$) and inserted into Eqn. (5.1).

We use for strain rate controlled experiments an ARES (TA Instruments) and for stress controlled experiments a MCR 500 (Anton Paar) rheometer. Both rheometers are equipped with a truncated cone-and-plate geometry (50 mm cone diameter, 17.45 mrad cone angle and 51 µm gap height). All measurements are performed at T =33 °C. At this temperature, the viscosity and density of the glycerol electrolyte (without dispersed particles) are η_s=500 mPas and ρ_s=1.05 g/cm^3, respectively. Then, secondary effects like particle inertia are avoided at strain rates $\dot{\gamma} < 10$ s^{-1}, because the particle Reynolds number $Re_p = \rho_s \dot{\gamma} a^2/\eta_s \approx 10^{-3}$ is much lower than 1 [18]. We also checked the absence of wall-slip.

5.3.3 Estimation of Yield Stress and Elastic Modulus

While we are dealing with dense suspensions, we expect the existence of a yield stress σ_y , i.e. a shear stress threshold with lower stresses than σ_y leading to elastically small deformations and higher stresses directly leading to irreversible large deformations. We are also interested in the elasticity of the suspensions, which is characterized by the elastic modulus G_0. Both measures are estimated in experiments with increasing shear stresses after Eqn. (5.1), replacing f by σ. The procedure to estimate σ_y and G_0 is visualized in Fig. 5.1 and is described as follows. We plot the shear strain γ as a function of the applied shear stress σ. Visual inspection of Fig. 5.1

reveals a kink in the curve of $\gamma(\sigma)$. At stresses below the kink, a linear relationship of γ on σ is clearly seen. We fit the data of this linear regime with a straight line. Next, we compare the measured data with the linear fit and define the first stress value, that deviates from the fit by more than 10% as the *static* yield stress σ_y. Moreover, we define the inverse of the slope of the fit line as the *linear* elastic modulus G_0.

5.3.4 Particle Surface Characterization

We investigate the surface composition of the particles with AFM imaging using a Nanoscope V (Veeco) in intermittent contact mode. The particles are deposited from dilute aqueous suspension onto a 2 µm syringe filter. Bare particles are compared with 2 and 8 layers. With the AFM, we record simultaneously height and phase images in the tapping mode at 0.8 Hz scan rate. We operate the AFM in the repulsive regime to avoid tip-sample contact. The used cantilever is a commercially available silicon (hydrophillic) Veeco OTESPA with tip radius 9 nm, resonance frequency 300 kHz and spring constant 42 N/m.

5.4 Rheological Experiments

5.4.1 Results of Applied Shear Stress

In this section, we study the solid-like behavior of the suspensions. We impose a shear stress $\sigma_0 = 10^{-3}$ Pa which we gradually increase after Eqn. (5.1) up to the final stress $\sigma_\infty = 10^3$ Pa. During the application of the shear stress, we record the resulting strain $\gamma(\sigma)$. The deformation curves, i.e. the plots of $\gamma(\sigma)$ versus σ, exhibit characteristic features of a solid-like material such as a linear stress-strain regime from which we obtain a static yield stress σ_y and a linear elastic modulus G_0 (see Sec. 5.3.3 for further details).

First of all we are interested in a possible evolution of the solid-like properties with increasing PEM layers. Hence, we plot in Fig. 5.2 the both measures σ_y and G_0 versus the layer number. The yield stress of suspensions with PSS terminated PEMs increases of one order in magnitude from layers 2 and 4 to layers 6, 8 and 10 with a mean value $\overline{\sigma}_{y,PSS} = 1.1$ Pa. The yield stress of PDADMAC terminated PEMs is $\overline{\sigma}_{y,PDAD} = 0.63\,\text{Pa} < \overline{\sigma}_{y,PSS}$. For comparison, we also plot the yield stress of bare particles $\sigma_y = 0.47$ Pa which is slightly lower than $\overline{\sigma}_{y,PDAD}$. The suspensions show qualitatively the same behavior for the elastic modulus G_0 as for the yield stress σ_y discussed before. We observe an increase of elasticity over 3 orders of magnitude for PSS terminated PEMs, until G_0 reaches a mean value $\overline{G}_{0,PSS} = 49$ Pa for layers 6, 8 and 10. The PDADMAC terminated PEMs show no increasing G_0 and the mean value $\overline{G}_{0,PDAD} = 16\,\text{Pa} <$

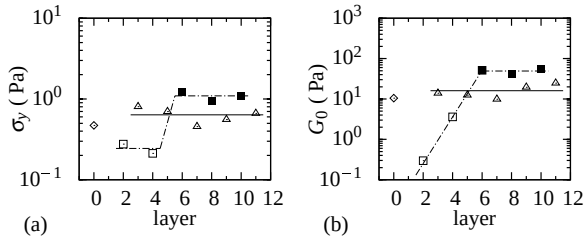

Figure 5.2: Solid-like properties of the suspensions; evolution of (a) yield stress σ_y and (b) elastic modulus G_0 with the number of polyelectrolyte layers. The lines in (a) and (b) serve to guide the eye (PSS terminated PEMs (squares), PDADMAC terminated PEMs (triangles) and bare particles (diamonds)).

$\overline{G}_{0,PSS}$. Bare particles are also plotted in Fig. 5.2(b) with an elastic modulus $G_0 = 11$ Pa slightly lower than $\overline{G}_{0,PDAD}$.

Another interesting feature appears when we perform stress hysteresis loops as plotted in Fig. 5.3(a) and focus on the small stress limit in the branch of the loop with decreasing shear stresses (gray). This region is plotted in Fig. 5.3(b). In this figure, we observe negative strain rates for PSS terminated suspensions with 6, 8 and 10 layers when the released shear stresses drop below a critical value of about 0.275 Pa. With further decreasing shear stresses, the strain rates remain at a constant value which corresponds to the linear stress-strain regime in the former tests with increasing imposed shear stress. Note that this critical stress is nearly one order of magnitude smaller than the static yield stress σ_y of the three suspensions. Hence, it becomes evident, that these suspensions store a certain amount of the elastic energy *during* the stress loading of the hysteresis loop. Such a change in the sign of the strain rate is indicative for a change in the rotational direction of the rheometer and was observed experimentally and numerically for suspensions with weakly attractive particles before [95, 96].

5.4.2 Results of Applied Strain Rate

After characterizing the solid-like properties of the suspensions, we focus now on the flow behavior. Therefore, we prescribe $\dot{\gamma}$ after Eqn. (5.1) and record σ. The resulting flow curves $\sigma(\dot{\gamma})$ (Fig. 5.4) show in general the same basic trend: starting at low $\dot{\gamma}$, the stress increases monotonically with increasing strain rate. As $\dot{\gamma}$ increases further, the suspensions show shear-thinning behavior, followed by a small Newtonian region at intermediate strain rates, 5×10^{-3} to 5×10^{-1} s^{-1}, and shear-thickening at high strain rates. The overall flow behavior is superimposed by a developing stress plateau at intermediate strain rates. The plateau stress value rises with increasing layer number. In addition, suspensions with 6, 8 and 10 layers show a maximum stress value after the monotonically stress increase, at $\dot{\gamma} \approx 5 \times 10^{-4}$ s^{-1}, then σ

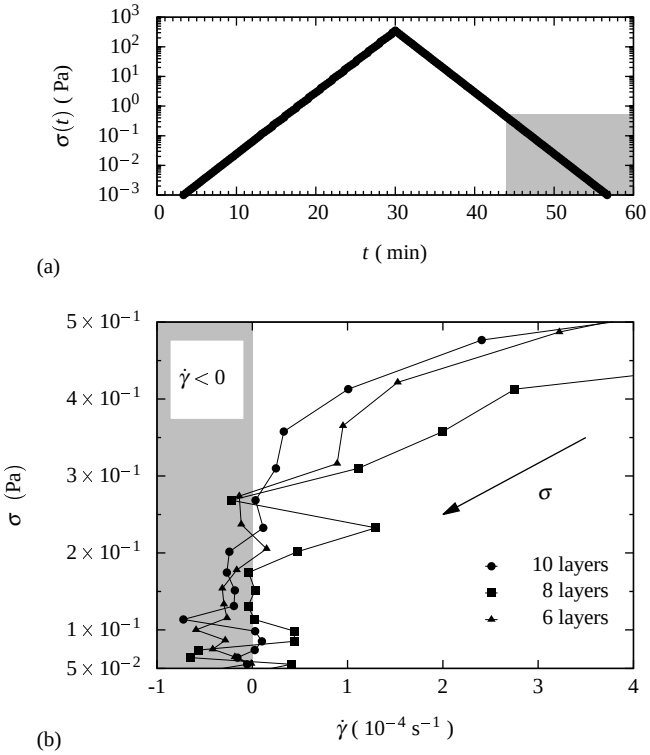

Figure 5.3: Imposed decreasing shear stress versus the strain rate. After performing a stress hysterises loop (a), the strain rates for PSS terminated suspensions with 6, 8, and 10 layers switch to negative strain rates when the applied stress drops below a critical value (b).

decreases, going through a minimum and increasing further, while $\dot{\gamma}$ increases for all times.

Such an occurrence of a maximum stress followed by a negative slope in the flow curves and/or a stress plateau clearly indicates a structural instability at the solid-liquid transition [25, 97]. The origin of this flow instability, may be the localization of the globally imposed strain rate $\dot{\gamma}$ in small, but highly sheared bands [98]. The onset of shear banding is triggered by a critical strain rate $\dot{\gamma}_c$. For $\dot{\gamma} > \dot{\gamma}_c$ the material flows entirely, while for $\dot{\gamma} < \dot{\gamma}_c$ material outside of the shear band is at rest and material in the shear band is sheared at a local strain rate $\dot{\gamma}_{loc} = \dot{\gamma}_c$. The transient nature of shear banding is generally independent from aging or thixotropy but is related to stress relaxation processes and one can define a fluidization time τ_f as the duration of the transient solid-liquid transition regime [99]. In our experiments, the ramp time τ_r in Eqn. (5.1) is then a measure how fast $\dot{\gamma}_c$ is reached and therefore τ_r gives evidence if the stress has enough time to relax or not.

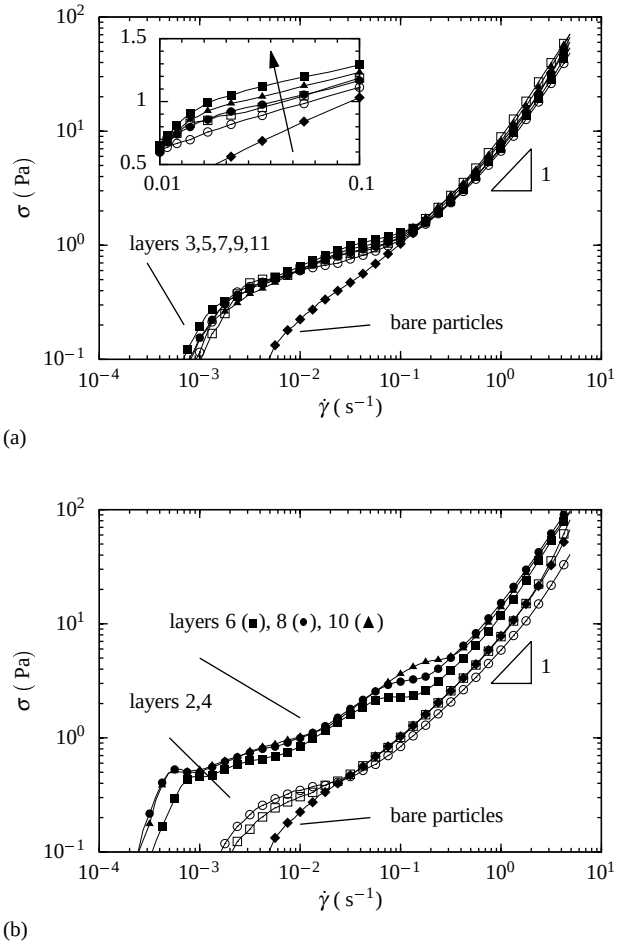

Figure 5.4: Start-up flow curves for all investigated suspensions; (a) PDADMAC and (b) PSS terminated PEMs. Inset in (a): An increasing layer number (arrow) lead to a developing stress plateau.

In the light of shear banding, we can interpret our flow curves as follows: i) Suspensions of bare particles and of particles with PEMs of 2 and 4 layers (PSS terminated PEMs) show no shear banding. The flow curves are strictly monotonically increasing. In this case, the stress relaxation is fast enough to reach a homogeneous flow state at every imposed $\dot{\gamma}$. ii) Suspensions with particles of PDADMAC terminated PEMs show the onset of shear banding with a developing stress plateau as seen in the inset in Fig. 5.4(a). The flow curve is now merely monotonically increasing. This is, because the stress cannot fully relax under shear, with τ_f comparable to the shear time. iii) Suspensions of particles with PEMs of 6, 8 and 10 layers (PSS terminated PEMs) show distinctive shear banding. The flow curve is non-monotonically

increasing. Now, the stress relaxation is much slower than the shear time and hence these suspensions have the longest τ_f.

A similar developement of transient shear banding is found in experiments of attractive colloids with increasing ϕ or τ_r [25, 99, 100]. The cause of such shear banding phenomena is the competition between aging and rejuvenation [97, 98, 100]. Because in our experiments ϕ and τ_r are constant, we speculate, that in our suspensions the PEMs alter the interaction potential U. This should result in altered aging and rejuvenation times. Unfortunately, no systematic study of the impact of U on shear banding is present so far, but it is interesting to note that the most shear-banding suspensions are the suspensions which showed the negative strain rates. This is fully in agreement with the experiments of Larsen *et al.* [95] and the simulations of Varnik *et al.* [96] whose systems also exhibited shear banding. We remember that the systems of these both works also showed negative strain rates as discussed in section 5.4.1.

5.5 Introducing a Measure for the Distinction between Precursor and Multilayer Regime

The physical picture that emerges from the features observed in the experimental section (yield stress, shear-banding) is that of a jammed system [10, 77]. In a jammed (solid-like) state, local elements form attractive links that can elastically deform, giving rise to the elastic modulus G_0, and bear certain amount of shear stress. The material yields after exceeding a maximum shear stress σ_y. Remarkably, in jammed colloidal suspensions, scaling the yield stress σ_y by the modulus G_0 takes on a single value for a specific particle type [74, 101–105]. It is known that the physico-chemical composition of the interface between PEM and solvent differs in the very first layers from layer to layer. Therefore, the quantity σ_y/G_0 may serve as a measure to investigate the layer dependence. To check this hypothesis, we plot σ_y/G_0 as a function of the layer number, as done in Fig. 5.5. Indeed, the value of σ_y/G_0 for bare particles is about twice the value of PEM modified particles. Moreover, σ_y/G_0 differs from layer to layer in the range up to 8 layers. The value of $\sigma_y/G_0 = 4.5 \times 10^{-2}$ of the bare particles is in good agreement with the experiments of Chow *et al.* [106] also using polystyrene latex particles.

The PEM modified particles show a clear layer dependence up to the 6th (9nth) layer for PSS (PDADMAC) terminated PEMs. For more layers, the scaling of the yield stress by the elastic modulus became independent of the layer number with $\sigma_y/G_0 = 2 \times 10^{-2}$ for PSS and $\sigma_y/G_0 = 2.75 \times 10^{-2}$ for PDADMAC terminated PEMs. From this observation, we conclude that well defined PEM interfaces need more than6 to 9 layers to be fully independent of the underlying substrate. Such a separation into a *precursor* regime with an ill-defined interface and a *multilayer* regime with well-defined interface is characteristic for PEM systems [4, 107].

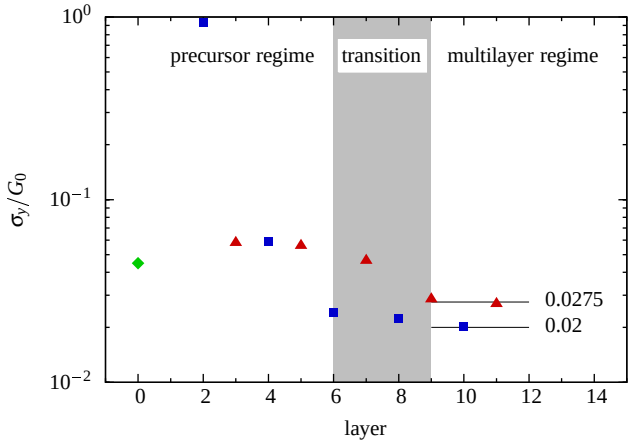

Figure 5.5: The scaled yields stress σ_y/G_0 as a function of the layer number (PSS terminated PEMs (squares), PDADMAC terminated PEMs (triangles) and bare particles (diamond)).

A possible cause for the strongly different values of σ_y/G_0 in the precursor regime, may be found in layer specific interaction potentials. The only experimental study on such multilayer dependent interaction potentials – to our knowledge – is found in the work of Bosio *et al.* [94]. There, it is shown that the interaction potential between PEM covered substrates exhibit a strong layer dependence in the precursor but is layer independent in the multilayer regime. In the precursor regime, strong adhesion occures which differs from the also attractive van der Waals contribution. The probability of the occurence of such strong adhesion events decreases with increasing layer number. For the first layer, this probability could easiliy reach about 50% which is not a small effect. This propability seems to decrease exponentially with increasing layer number [107]. For strong adhesion events, the magnitude of the mean adhesion energy depends on the terminating PE, which supports the odd-even-effect as seen in our rheological measurements. This is likely due to the charge density or hydrophobicity of the PE backbone of the terminating PE [108–110].

Using AFM images of the PEM surface, Bosio *et al.* [94] relates the strong adhesion events to local topography inhomogeneities. According to [94], we also use AFM imaging to examine the particles surface heterogeneity. Fig. 5.6(a) shows 500x500 nm height images of the pole of bare particles and particles with 2 and 8 layers, respectively, representative for the precursor and multilayer regime. These images indicate a heterogeneous surface topography of bare particles, while with increasing layer number the topography gets more homogeneous. This is in excellent agreement of height images published in [94]. Remarkably, particles in the precursor regime exhibit clearly visible holes, which can be quantified by the power spectral density (PSD). In the plot of the power spectral density (PSD) in Fig. 5.6(b), it is clearly seen that the precursor length scale ranges from $k^{-1} = 10$ to 50 nm. At this length scale, the PSD value is dominated by particles with 2 layers. This finding supports the visual inspection of the

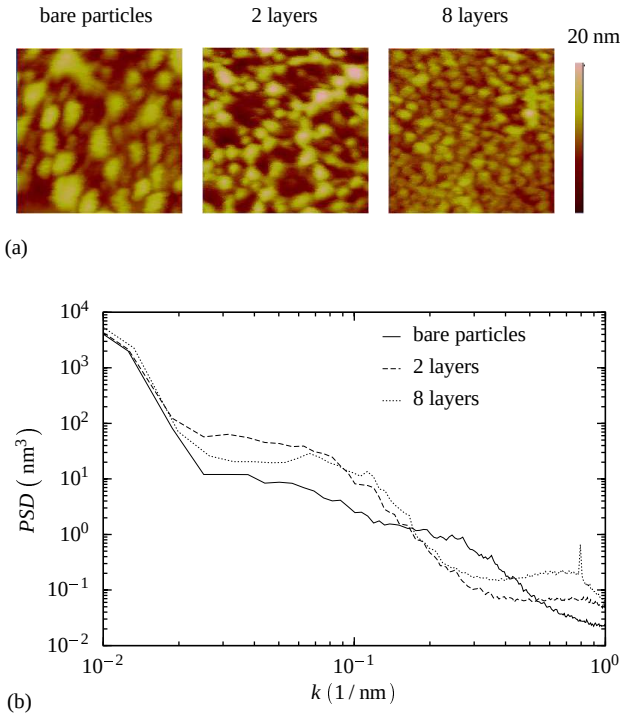

Figure 5.6: Particle surface characterization. (a) AFM height images of bare particles (left) and of PEM coated particles with 2 (middle) and 8 (right) layers. The size of the images is 500x500 nm. The scale bar indicates the height. (b) Power spectral density PSD versus the spatial frequency k.

AFM images. The mentioned features seem to diminish in the multilayer regime resulting in a more homogeneous surface topography as the PSD value at small wavelength is dominated by the 8 layer PEMs. This is what is seen in the corresponding AFM images of Fig. 5.6(a), where the surface for the 8 layer PEM is covered by the finest structures. From such a homogeneous surface, we expect the absence of the discussed strong adhesion and consequently a layer independent scaling σ_y/G_0. Hence, the AFM images confirm the scaling behavior in Fig. 5.5.

5.6 Origin of the Scaling

The previously described strong adhesion effects might have a strong impact on the mechanical properties of the microstructure of the suspensions. Therefore, we like to draw a first schematic of the interaction potential which should motivate for further investigations. In this schematic,

we describe the particle interaction potentials of bare particles and particles in the multilayer regime by the Derjaguin-Landau-Verwey-Overbeek (DLVO) theory $U = U_{vdW} + U_e$ [94] as the sum of van der Waals attraction [38]

$$U_{vdW}(r) = -\frac{aA_H}{12r}, \tag{5.2}$$

and electrostatic repulsion [111]

$$U_e(r) = \frac{4\pi\varepsilon a(r+a)\Psi_0^2}{r+2a} \ln\left[1 + \frac{a}{r+a}\exp(-\kappa r)\right]. \tag{5.3}$$

In Eqn. (5.2), $A_H = 3.8 \times 10^{-21}$ J is the Hamaker constant for polystyrene spheres across glycerol solvent [112] and r the separation distance between opposing particles. In the calculations, the surface potential Ψ_0 in Eqn. (5.3) is replaced by the measured ζ-potential. In this equation, the permittivity $\varepsilon = 3.8 \times 10^{-10}$ F/m and the Debye length $\kappa^{-1} = 2$ nm of the used glycerol electrolyte are calculated based on the data given in [113]. For the multilayer regime, Fig. 5.7 depicts the calculated interaction potentials based on the ζ-potential of bare and PSS terminated particles, $\zeta = -55$ mV, and for PDADMAC terminated particles, $\zeta = +25$ mV. The calulated DLVO potentials provide a weak attraction with $U(r)/k_BT \approx -10$.

As mentioned before, the potentials of the strong adhesion events that occure in the precursor regime can not be described by DLVO theory. However, recent works [114] related the additional attractive interaction potentials to electrostatic patch-charge attractions [115]. These patch-charge attractions can be described by a generic electrostatic potential [116]

$$U_{pc}(r) = -A\exp(-qr). \tag{5.4}$$

In Eqn. (5.4), A is the amplitude of the additional attractive interactions and q^{-1} their decay length. At low ionic strength, q^{-1} is governed by the size of the patches [114, 115], wheras at high ionic strength q^{-1} equals the Debye length κ^{-1} [115]. Because of the medium ionic strength of 10^{-2} mol/l NaCl in our experiments, we fix $q^{-1} = 10$ nm as the characteristic length scale of the precursor regime. We slightly vary A to study the change of the extended interaction potenial $U = U_{vdW} + U_e + U_{pc}$ with increasing charge heterogeneity, depicted in Fig. 5.7 for $\zeta = -55$ mV.

With increasing heterogeneity, the minimum of U grows while the range of U remains nearly unchanged. This observation is at odds with the experiments [74, 101–105] and should be the cause that in the precursor regime the quantity σ_y/G_0 differs from layer to layer. Hence, scaling the yield stress by the elastic modulus serves as a useful measure to estimate the extension of the precursor regime by macrorheological methods.

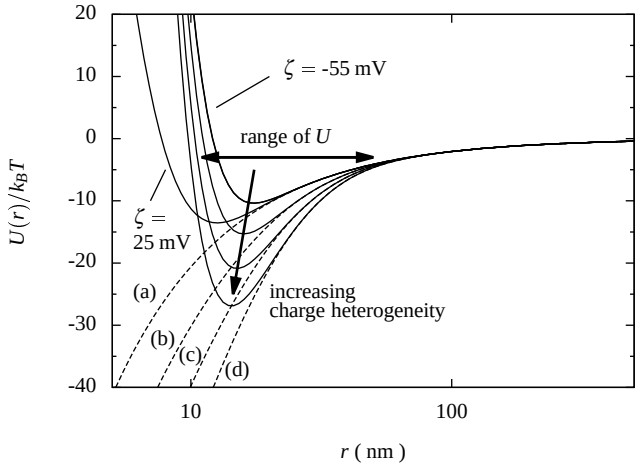

Figure 5.7: Calculated interaction potential $U(r)/k_BT$ (solid lines) as a function of the separation distance r with increasing charge heterogeneity using $A = 0$ (a), $A = 5 \times 10^7$ (b), $A = 1 \times 10^8$ (c) and $A = 5 \times 10^8$ (d). The dashed lines depict the corresponding attractive contributions $U_{vdW} + U_{pc}$.

5.7 Conclusions

Particle modification by polyelectrolyte multilayers provides a new way to influence the rheology of colloidal suspensions. The advantage of this approach is its applicability to a broad class of particles, since no specific surface chemistry but only a sufficiently high charge density is required. We show, that particle coatings with PEMs, assembled at high ionic strength, lead to electrosterically stabilization of colloidal suspensions and an increase of elasticity and yield stress. Furthermore, the terminal polyelectrolyte of the PEM alters the suspension behavior in a very subtle way; the occurence of a precursor regime locally induces additional attractive forces that make the suspensions more brittle. We establish a first guideline for the number of coating steps that are necessary in order to leave the ill-defined precursor regime and enter the well-defined multilayer regime, in which rheological properties become largely independent surface properties of the original particles. These promising results provide a basis for a deeper understanding of the underlying physical mechanisms. Such an understanding could be achieved by the correlation of interaction potentials which can be determined using Colloidal Probe (CP) AFM.

6

Viscoelasticity and Shear Thickening of Polyelectrolyte Multilayer Modified Colloidal Suspensions

6.1 Abstract

The adsorption of brushy polyelectrolyte multilayers (PEMs) onto micron sized particles offers an interesting alternative to manipulate the macroscopic behavior of the rheology of dense suspensions. Using oscillatory and steady shear experiments, we present a systematic study of the relationship between PEM modification and rheology. On the microscopic level, the film properties are determined by the outermost polyelectrolyte of the PEM film, which affects surface charge and porosity. Both properties change with layer number, which is known as the odd-even effect. At the macroscale, the odd-even effect is observed in the viscoelastic measures, and is most pronounced at the onset of shear thickening. The shear thickening stress reveals remarkable scaling as the surface charge and porosity of the PEMs are varied. Hydroclusters are the origin of shear thickening and the interplay of elastic interparticle and viscous hydrodynamic forces dictate the mechanical response in high shear. Scaling the viscoelastic measures by the dominant stress and time scales, leads to a surprising collapse of the data onto universal master curves in the elastic and shear thickening regime.

6.2 Introduction

Surface modification of colloids is essential for many applications in industry and basic research. Modified colloids of the core-shell type consist of soft polymers grafted or adsorbed onto a solid core [117–120]. An effective alternative pathway designing highly functionalized shells is via polyelectrolyte multilayers [7, 8, 81].

Polyelectrolyte multilayers (PEMs) are nanoscale-thin films, consisting of alternating layers of polyanions and polycations where each polyelectrolyte layer renders the surface charge to the opposite [121]. A famous method for PEM film creation is the layer-by-layer (LbL) self assembly technique proposed by Decher in the mid 1990s [80]. As the main benefit, PEMs create a template independent interface with unique physicochemical properties when exceeding only a few layers [44]. Therefore, PEM surface modification became established as a versatile tool for tuning the interfacial properties of a wide variety of materials for technical, medical and biological applications at the molecular scale [4, 122, 123]. The behavior of the newly created interface can be fine-tuned by different stimuli such as temperature, pH and ionic strength of the surrounding medium.

In many application fields, PEM modified colloids are dispersed in an aqueous medium. The essential macroscopic parameters are dispersion stability and rheology [124–126]. Although a considerable amount of works concerning PEM modified colloidal suspensions deal with stability issues [127–129], little is known about their macroscopic behavior in rheology.

A recent study on dense PEM modified suspensions investigates the variation of the polyelectrolyte conformation within the multilayer using steady shear [130]. Brushy PEMs proved to significantly enhance the yield stress while the viscoelastic scaling remains valid. A previous study focuses on brushy polyelectrolyte multilayers and found the existence of a precursor regime for thin PEM films up to layers 5 or 6 where the elasticity and the yield stress are still influenced by the colloidal template [131]. In the multilayer regime, both properties became independent of the layer number and elasticity and yield stress values are solely determined by the outermost polyelectrolyte of the PEM film. Moreover, it was found that the rheological properties also depend on the type of polyelectrolyte that terminates the multilayer.

In contrast to this previous study, herein we explore the effect of the terminating polyelectrolyte in oscillatory and steady shear experiments. We study brushy PEMs, made up from poly(diallyldimethylammonium chloride), PDADMAC, and poly(sodium styrenesulfonate), PSS, as a function of terminating polyelectrolyte. The used polyelectrolytes form one of the most studied polyelectrolyte complexes, with both polyelectrolytes are strongly dissociated over a wide range of pH values. In the multilayer regime, the thickness of these (PDADMAC/PSS) PEMs grows linearly with layer number [132, 133]. The total film thickness, L_p, of the highest layer numbers studied herein is about 100 nm [44, 134]. We assemble the PEMs

onto monodisperse polystyrene particles with mean radius $a = 2.5$ µm. Hence, the effective particle radius, $a_{eff} = 1 + L_p/a$, changes with increasing layer numbers to less than 2%, and throughout the work, therefore we treat the particle volume fraction, ϕ, as constant [135, 136]. This allows us to investigate the effect of the terminating polyelectrolyte unaffected by volume fraction changes, which we fix in the present study to $\phi = 0.55$. With the adjusted volume fraction and layer thickness, we match the conditions of the experiments and numerical studies that concern shear thickening of core-shell particles [137–139].

Using complementary oscillatory and steady shear experiments, we show the impact of the terminating polyelectrolyte on the rheology of polyelectrolyte multilayer modified colloids. We present several scalings and develop a first picture of the very complex nature of this relatively new class of core-shell particles.

6.3 Materials and Methods

Materials and Chemicals. Monodisperse, negatively charged polystyrene particles, zeta potential $\zeta = 55$ mV, with $a = 2.5$ µm radius served as templates for the alternating adsorption of single polycation, PDADMAC, and polyanion, PSS, layers. Details of particle synthesis and characterization are described in [131]. The polyelectrolytes, poly(diallyldimethylammonium chloride) (PDADMAC, $M_w = 100\,000 - 200\,000$ g/mol) and poly(sodium styrenesulfonate) (PSS, $M_w = 70\,000$ g/mol), along with sodium chloride (NaCl) and glycerol ($\geq 99\%$), were purchased from Aldrich and used without further purification. All solutions were prepared with ultra pure water, provided by a Milli-Q Ultrapure Water System (Millipore).

Polyelectrolyte Multilayer Fabrication. Polyelectrolyte multilayers are assembled via a LbL self-assembly technique [4, 80]. Therefore, polyelectrolytes were dispersed in excess concentration in aqueous deposition solutions [6]. To achieve a brush-like polyelectrolyte conformation, the multilayer formation takes place at high ionic strength. Hence, the deposition solutions were adjusted to 1 mol/L NaCl [140]. Particles were dispersed in the deposition solution under permanent stirring. The PEs were allowed to adsorb for 30 min, permanently shaking the deposition solution. After each adsorption step, the particles were washed three times with ultra pure Milli-Q water by centrifugation, decanting the supernatant, and redispersing in fresh water. Polyelectrolyte adsorption was repeated several times to obtain particle batches covered with PEM films from 2 to 11 layers. After multilayer assembly, the particles were dried in a vacuum chamber at 30 °C. Charge reversal during multilayer assembly was followed by ζ-potential measurements performed on a Zetasizer Nano ZS (Malvern). The PDADMAC terminated samples yield a surface charge of $\zeta = +25$ mV, whereas bare and PSS terminated samples have $\zeta = -55$ mV.

Suspension preparation. Dry particles were weighted and milled at high shear into glycerol

electrolyte at volume fraction of $\phi = 0.55$. The ionic strength of the glycerol electrolyte was previously adjusted to 10^{-2} mol/L by adding NaCl.

Mechanical Characterization. The rheological experiments were performed on a strain controlled ARES (TA Instruments). The rheometer was equipped with a truncated cone-plate geometry of 50 mm diameter, and a convection oven that operates at 33 °C. A pre-shear protocol was applied prior to each measurement with 180 s oscillatory shear at strain amplitude $\gamma_0 = 5$ and frequency $\omega = 2\pi$ rad/s, followed by 180 s stress relaxation at zero strain. This protocol leads to reproducible results.

6.4 Results and Discussion

Viscoelasticity. We basically restrict our study to the multilayer regime. However, sometimes it is instructive to incorporate observations from the precursor regime as well. We investigate PEM modified suspensions at volume fraction $\phi = 0.55$, where they behave as viscoelastic materials, which we determined by oscillatory shear experiments at constant frequency, $\omega = 2\pi$ rad/s, and strain amplitudes ranging from about $\gamma_0 = 5 \cdot 10^{-4}$ to $5 \cdot 10^{0}$. We measure the responding stress amplitude, σ_0, and phase lag, δ, from which we estimate the elastic, G', and viscous, G'', moduli [18].

The suspensions respond linear viscoelastic up to yield strains of about 10^2, indicated by values of the phase angle, δ, around $\pi/4$, as seen in Fig. 6.1. Typical values for the linear viscoelastic moduli are $G' = 10^2$ Pa and $G' = 2 \cdot 10^1$ Pa, respectively for PSS and PDADMAC terminated samples. The suspensions start yielding at yield strains around $\gamma_y \approx 10^{-2}$. Exceeding γ_y, the suspensions respond more and more non-linearly to the applied strain and the measured data reveal, shear thinning, Newtonian, shear thickening, and 2nd Newtonian regimes. The strong dissipation in the Newtonian and 2nd Newtonian regimes are marked by a δ close to $\pi/2$. In the other two regimes, shear thinning and thickening, the suspensions become more elastically with $\delta < \pi/2$.

Energy Dissipation Shear thickening is accompanied by increasing energy dissipation. The dissipated energy per cycle and volume is [26]

$$E_d = \int_0^{2\pi} \sigma(\gamma)\, \mathrm{d}\gamma = \pi G'' \gamma_0^2 \,. \tag{6.1}$$

In the linear regime, $E_d \propto \gamma_0^2$, and Fig. 6.2 supports our previous observation that the suspensions behave linear viscoelastic up to $\gamma_0 \approx 2 \cdot 10^{-2}$. In the following Newtonian regime, the bandwidth of the set of E_d-curves narrows down to a minimum at $\gamma_c \approx 3 \cdot 10^{-1}$. At this critical strain, the curves nearly collapse onto a single data point. This behavior is evident because in the Newtonian regime, the microstructure aligns under increasing shear and due

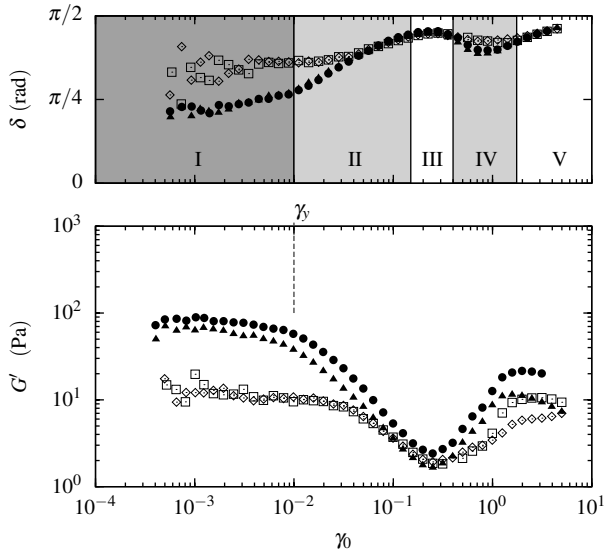

Figure 6.1: Oscillatory shear data as function of strain amplitude, γ_0. The upper and lower panel show respectively phase angle, δ, and elastic modulus, G'. The solid and open symbols denote samples with PSS and PDADMAC terminated polyelectrolyte multilayers, respectively. Plotted are representative data for the multilayer regime with PEMs of 8 (circles), 9 (squares), 10 (triangles), and 11 (diamonds) polyelectrolyte layers. Several rheological regimes are highlighted: I) linear viscoelastic, II) shear thinning, III) Newtonian, IV) shear thickening, and V) 2nd Newtonian plateau.

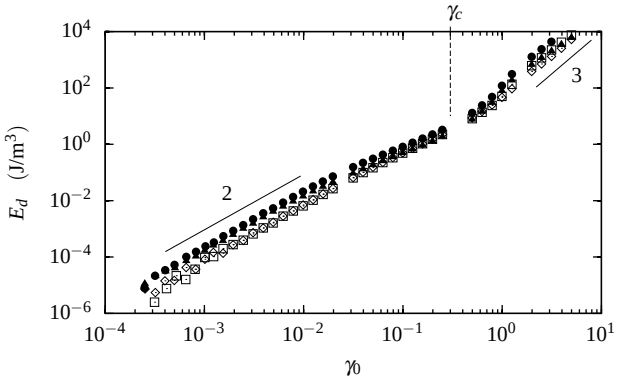

Figure 6.2: Dissipated energy, E_d, during oscillatory shear as a function of γ_0 examplified by PEMs of 8 (circles), 9 (squares), 10 (triangles), and 11 (diamonds) polyelectrolyte layers.

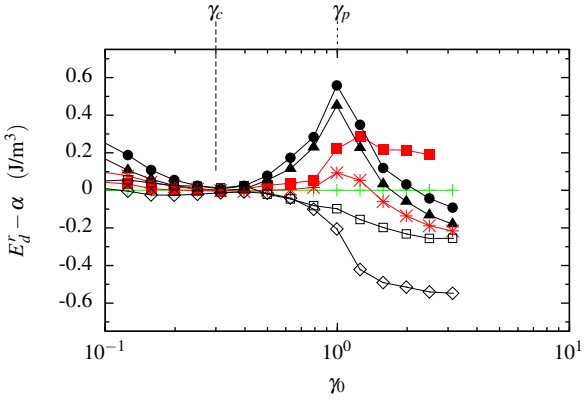

Figure 6.3: Representative data of the relative energy dissipation, $E_d^r = E_d^{coated}/E_d^{bare} - 1$, for PEMs of 8 (circles), 10 (triangles), 2 (squares), 3 (stars), 9 (open squares), and 11 (open diamonds) polyelectrolyte layers. For comparison, data of bare particles (crosses) are also plotted. Please note that the curves are shifted vertically by the factor α to match zero at the critical strain, $\gamma_c = 3 \cdot 10^{-1}$.

to the fixed particle size and volume fraction, E_d should reach a unique value for all samples [138, 141, 142]. Exceeding the critical strain, γ_c, the dissipated energy jumps over one decade before arriving at an exponential growth with a slope 3.

To investigate the transition from Newtonian flow to shear thickening around γ_c in more detail, we compare the dissipated energy, E_d^{coated}, of the PEM modified suspensions with that of bare particles, E_d^{bare}. Therefore, we propose a relative dissipated energy, $E_d^r = E_d^{coated}/E_d^{bare} - 1$, which we plot in Fig. 6.3 as a function of γ_0.

Besides the onset of shear thickening at γ_c, there appears another distinguished strain value, $\gamma_p = 10^0$, where the different layer numbers and polyelectrolyte terminations lead to a surprising evolution of the trace of E_d^r. Thick films (high layer numbers) with PSS termination show a sharp peak at γ_p. This peak vanishes with decreasing PSS and increasing PDADMAC film thickness (layer number). Thus, traces of thin films adapt the straight line of the bare particles. Instead of the peak, thick films of PDADMAC terminated samples undergo a stepwise transition to shear thickening. All traces tend to a plateau at $\gamma_0 > 3 \cdot 10^0$, which coincides with $E_d \propto \gamma_0^3$.

We interpret these results in terms of the dependence of the physicochemical interface properties between the terminating polyelectrolyte and the background fluid on the film thickness. Thin films with less than 5 to 6 layers have a heterogeneous surface and the interface properties are still influenced by the surface properties of the colloidal template [4, 94, 131]. This explains why traces of E_d lie close to that of bare particles. As the film thickness increases, the impact

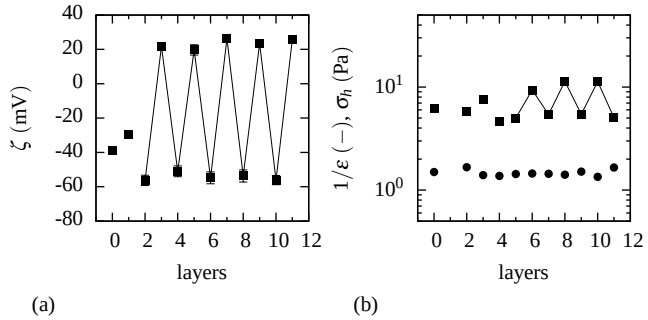

Figure 6.4: Surface charge in terms of ζ-potential (a), as well as (b) extra stress, σ_h (squares), and slope, $1/\varepsilon$ (bullets) versus layer number. The *odd-even* effect is highlighted by the solid lines.

of the colloidal template on the PEM/background fluid interface vanishes, and for thick films, ≥ 6 layers, the interface properties are solely determined by the terminating polyelectrolyte. This dependence on the terminating polyelectrolyte is known as the odd-even effect for several microscale external and internal multilayer properties like surface charge (see Fig.4(a)), surface energy, and solvent content of the multilayer film [4, 109, 124, 143].

Shear Thickening. The surprising existence of a characteristic strain, γ_p, motivates steady shear experiments to further investigate the transition to shear thickening. For this, we measure the responding shear stress, σ, of descending applied strain rates, $\dot{\gamma}$, and detect the regimes II–V as observed in the oscillatory shear experiments given by Fig. 6.1. The resulting flow curves, $\sigma(\dot{\gamma})$, can be modeled as [138, 144–146]

$$\sigma(\dot{\gamma}) = \sigma_y + \sigma_l \dot{\gamma}^{1/2} + \sigma_h \dot{\gamma}^{1/\varepsilon} \,, \tag{6.2}$$

wherein σ_y denotes the dynamic yield stress below which the samples behave predominantly elastically, as detected in oscillatory shear, Fig. 6.1. The extra stress in the shear thinning and shear thickening regime is parameterized by σ_l and σ_h, respectively, and $1/\varepsilon$ refers to the slope in the shear thickening regime. Equation (6.2), correctly reproduces our experimental $\sigma(\dot{\gamma})$ data. We focus on the transition to shear thickening, characterized by the high rate extra stress, σ_h. We plot σ_h in Fig. 6.4(b) as a function of polyelectrolyte layer number. Remarkably, σ_h and E_d^r demonstrate qualitatively similar layer dependence: values of σ_h lie close to that of bare particles for thin films with < 5 layers and show a distinct odd-even effect for thick films with layers ≥ 5. Interestingly, the slope of the flow curves, $1/\varepsilon$, is independent of the terminating polyelectrolyte. This finding seems to be a general feature of dense suspensions, and implies that the slope of the flow curves is independent of the strength of attractive interparticle interactions [146].

Since the transition to shear thickening is known to be a sensitive probe for interparticle interactions [20], it is likely that this *rheologically observed* odd-even effect is linked to the *mi-*

croscopically observed odd-even effect obvious from ζ-potential measurements [4, 94, 131]. Furthermore, the origin of the continuous shear thickening is due to the formation of hydroclusters [142, 147–149]. The aggregation of particles to hydroclusters is the consequence of a delicate interplay between interparticle and hydrodynamic interactions. Such interactions mediate the approach or separation of particles which are in close proximity [146, 150, 151]. Because of the obvious link between ζ-potential and σ_h, we suppose that the electrostatic component of the interparticle interactions dominates the repulsive interactions. Hence, at the transition to shear thickening, the electrostatic force,

$$F_e = 2\pi\varepsilon_0\varepsilon_r\psi_0^2\ \kappa a/2\,, \tag{6.3}$$

and the hydrodynamic force,

$$F_h = 6\pi a^2\sigma_h\, k(h,\delta_p^{-1},L_p)\, a/h\,, \tag{6.4}$$

have to be in balance [152, 153]. In Eqn. (6.3), ε_0 and ε_r, respectively denote the permittivity of free space and particle, and κ the inverse Debye length over which F_e yields a significant contribution to the interparticle interactions; the surface charge, ψ_0, can be replaced by the measured ζ-potential. We consider the polyelectrolyte multilayers as porous shells [154, 155], which are known to enhance lubrication [156]. Thus, we had to extend Eqn. (6.4) by $k(h,\varphi^{-1},L_p)$, with the interparticle distance h, hydrodynamic permeability φ, and shell thickness L_p [138, 157–160].

At the onset of shear thickening, both forces have to be equal, and the shear stress is [145]

$$\sigma_h = \frac{\varepsilon_0\varepsilon_r\kappa}{6a^2}\,\frac{\zeta^2}{k}\,h\,. \tag{6.5}$$

Assuming constant h and L_p for all samples results in $k(h,\varphi^{-1},L_p)\propto\varphi^{-1}$ [138, 157–160]. Hence, overall, we expect σ_h to scale as

$$\sigma_h \propto \zeta^2\varphi\,. \tag{6.6}$$

To our knowledge, there are no experimental values of φ avaible, and thus we replace φ with a generic shift factor a_φ. We plot in Fig. 6.5 values of σ_h as a function of $\zeta^2 a_\varphi$. The resulting curves can be superimposed by using shift factors a_ϕ close to 4 and 2, respectively, for PDADMAC and PSS termination. The shift factors are chosen to collapse the data of the PEM modified samples onto that of bare particles. The scaling of our data is in good qualitative agreement with findings from nano-filtration experiments performed on multilayer membranes composed of PDADMAC and PSS [161–163]. These experiments report on PDADMAC terminated multilayer membranes, which yield an about two times higher glycerol flux than through PSS terminated multilayer membranes. The origin of the higher glycerol flux is the lower ionic cross-link density of the PDADMAC terminated PEMs.

Characteristic Stress and Time Scales. In our emerging picture, particles are in close proximity either at rest when elastic interparticle interactions dominate the microstructure, or at

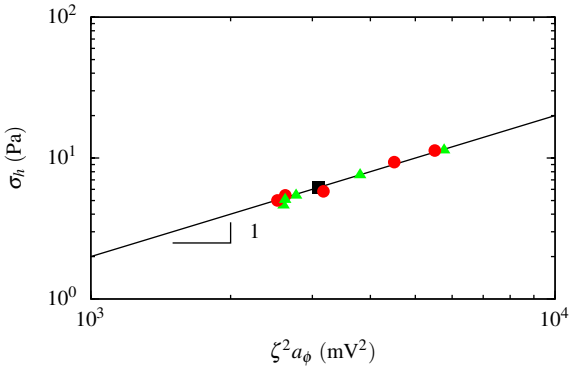

Figure 6.5: High shear extra stress, σ_h, as a function of ζ-potential, rescaled according to Eqn.(6.6) using $\varphi \propto a_\varphi$. Plotted are data for bare particles (square), and particles with PDADMAC (triangles), and PSS (circles) termination. The solid line is a fit of Eqn.(6.6) to the data.

high strain rates when dissipative hydroclusters modify the flow properties of the suspensions. To separate these effects, we decompose the measured shear stress amplitude in an elastic, $\sigma_0'' = \sigma_0 \sin\delta$, and viscous, $\sigma_0' = \sigma_0 \cos\delta$, part [164].

In the linear viscoelastic regime, the elastic stress dominates the stress scale. Then, the stress and time scale are determined by σ_y and η_∞/G_0, respectively [102]. Normalizing the stress and the shear time, $1/\dot{\gamma}$, by these values lead to the master curve plotted in Fig. 6.6(a). To highlight the universality of this scaling, we used values of σ_y and linear elastic modulus, G_0, from independent experiments with applied shear stress [131].

In the shear thickening regime, the viscous stress dominates the stress scale. Then, σ_h sets the

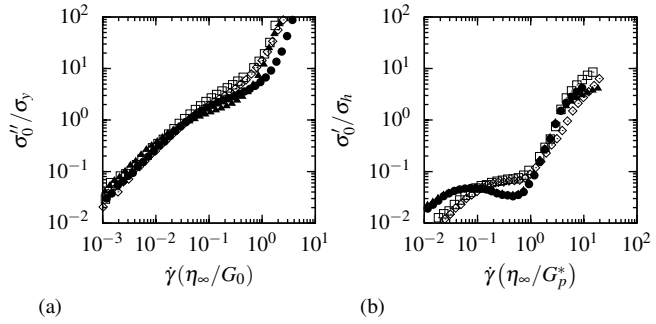

Figure 6.6: Stress decomposition in (a) reduced elastic and (b) reduced viscous stress respectively as function of the dimensionles strain rate.

stress scale during shear thickening. The previously discussed extension and compression of particles within the hydroclusters suggests, that both, elastic and viscous components, enter the characteristic time scale [142, 147]. Hence, we use the complex modulus, $G^* = G' + \mathrm{i}G''$, as viscoelastic measure, and normalize the strain rate by η_∞ / G_p^*, with values of G_p^* determined at γ_p. Figure 6.6(b) shows the dimensionless viscous stress as function of dimensionless strain rate. Remarkably, in the shear thickening regime, between 10^0 and 10^1, all date collapse onto a single curve.

6.5 Summary and Conclusions

At high volume fraction, (PDADMAC/PSS) multilayer modified colloids are nonlinear viscoelastic materials. Below a yield strain, γ_y, or yield stress, σ_y, they respond predominantly elastically with an elastic relaxation time, η_∞ / G_0, that is typical for dense suspensions. After the yield point, they shear-thin and finally enter a Newtonian flow regime. This yield transition is accompanied by a minimization of dissipated energy. Further increasing shear results in continuous shear thickening and rising energy dissipation. Thereby, continuous shear thickening introduces an other stress and time scale, determined by the stress at the transition to shear thickening, σ_h, and a hydrodynamic relaxation time, η_∞ / G_p^*. Due to the complex core-shell configuration of the polyelectrolyte multilayer modified colloids, the shear thickening is an elusive competition between interparticle and hydrodynamic forces. In a first approximation, the transition to shear thickening can be modeled by balancing the dominating interparticle with the hydrodynamic force, where the hydrodynamic force strongly depends on the permeability of the multilayer shell.

The variation of the film thickness reveals that thin films suffer from the surface properties of the underlying particle. In this case, the macroscopic behavior of the suspension is not well-defined. For the technologically more important thick films, the yield and flow behavior is strongly determined by the terminating polyelectrolyte of the multilayer film. Poly(sodium styrenesulfonate) termination results in more elastic and stronger dissipative colloids. Also, the stress at the transition to shear thickening, σ_h, is roughly two times higher than for PDADMAC termination. Moreover, PSS terminated films are also more permeable.

To conclude, polyelectrolyte multilayer modified colloids are promising core-shell particles as they allow to manipulate their macroscopic behavior in rheology, simply by changing the terminating polyelectrolyte layer. Particularly for thin films, more theoretical and experimental work has to be done to understand the correlation between microscopic and macroscopic measures in more detail.

7

Effect of Polyelectrolyte Conformation

7.1 Abstract

The yield stress of polyelectrolyte multilayer modified suspensions exhibits a surprising dependence on the polyelectrolyte conformation of multilayer films. The rheological data scale onto a universal master curve for each polyelectrolyte conformation as the particle volume fraction, ϕ, and the ionic strength of the background fluid, I, are varied. It is shown that films with highly coiled, brush-like polyelectrolytes significantly enhance the yield stress. Moreover, the polyelectrolyte multilayer modification changes the interaction strength, U, similar to I, leading to an unexpected scaling behavior.

7.2 Introduction

Control over the yield stress of colloidal suspensions is crucial for many industrial processes and basic research, including soft matter physics, materials engineering, food- and biotechnology [82, 165–168].

Colloids per se have great potential as building blocks for functional nanostructures [169, 170], but often lack essential features like biocompatibility, dispersibility, or sedimentation stability in aqueous and ionic media [171–173]. To improve their applicability, the surface of the colloids has to be functionalized [174]. Due to their huge internal surface, nanometer thin poly-

electrolyte multilayer (PEM) films, which are composed of alternating polyanion and polycation layers, are interesting materials for surface functionalization [4, 122, 175, 176]. Thereby, the physicochemical properties of the PEM films greatly benefit from the polymeric and ionic nature of the polyelectrolytes, and are mainly determined by the terminating polyelectrolyte layer.

The physicochemical properties of the PEM film, like hydrophobicity, porosity, surface charge and roughness, can be precisely adjusted by pH and ionic strength during PEM film assembly [4, 81, 177]. For example, increasing ionic strength during multilayer formation results in rougher PEM films [178]. Herein, we use two of the most studied strong polyelectrolytes, poly(diallyldimethylammoniumchloride) (PDADMAC) and poly(styrenesulfonate) (PSS), to create the multilayer films. Strong polyelectrolytes completely dissociate in aqueous media for wide range of pH values. Thus, the conformation of the used polyelectrolytes depends on their chemical structure and on the ionic strength. We systematically vary the conformation of the polyelectrolytes during PEM film assembly, and study the effect of the polyelectrolyte conformation on the dynamic yield stress, which proves to be a well-defined material property [179]. The polyelectrolyte conformation is, to a large extend, set by the salt concentration of the aqueous *deposition* solution [180]. Due to counterion screening, high salt concentrations, $c > 0.5$ M, lead to highly coiled, brushy polyelectrolytes with linearly growing film thickness [181]. Contrary to high salt concentrations, adsorption from salt free or low salt concentrations $c \leq 0.5$ M, results in flatly adsorbed polyelectrolytes which build comparatively thinner films [178]. Via the polyelectrolyte conformation, the salt concentration also moderates the roughness of the PEM film. The roughness of the PEM film increases with increasing brushiness of the polyelectrolyte building blocks [178]. As a main advantage, the polyelectrolyte conformation, and thus the roughness of the PEM film, is conserved, when the PEMs are transferred from the deposition solution to another aqueous medium [182]. Furthermore, the PEM films are kinetically stable for ionic strengths of the background fluid up to $I \approx 1$ mol/L monovalent salt [45, 183, 184]. This should allow us to tailor the interparticle interactions, and consequently the dynamic yield stress, ex situ, that is independent of pH and ionic strength of the background fluid [92, 185]. In contrast, competing surface functionalization approaches result in a strong coupling to the chemical composition of the background fluid.

While many applications require the dispersion of PEM modified colloidal particles in liquid media, and even though the use of PEMs as particle coating is often mentioned as a tool to stabilize colloids in suspension [6, 186], only a few works deal with the rheology of polyelectrolyte multilayer modified suspensions. In a previous work [131], we investigated the dependence of the static yield stress [12, 14, 15, 179] of dense suspensions on the number of adsorbed polyelectrolyte layers. The surface roughness decreases with increasing layer number, which is exemplarily visualized by Fig. 7.1 for PEM modified particles with 2 and 8 polyelectrolyte layers. The static yield stress becomes independent of the surface properties of the colloidal template when the PEM film consists of more than about 6 layers [131]. In this multilayer regime, the interparticle interactions are solely determined by the terminating polyelectrolyte layer. While this first study validated the capability of PEM modified suspen-

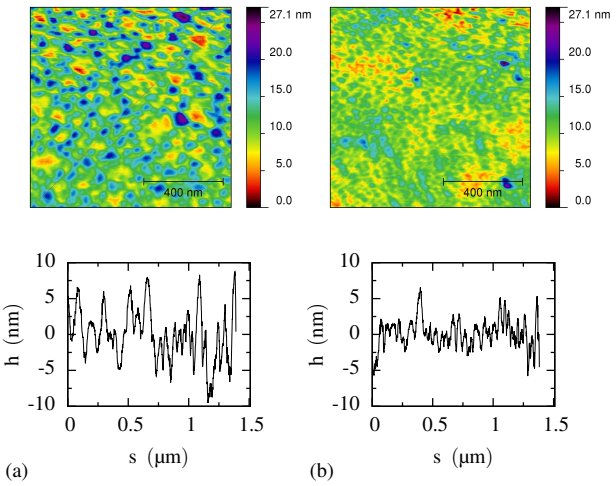

Figure 7.1: Topography images of PEM modified particles with 2 layers, (a), and 8 layers, (b). In the bottom row are the height profiles along the solid lines drawn in the topography images shown.

sions, a more detailed picture of the micro-macro interaction mechanism is essential for further applications.

With the present work, we take advantage of our previous findings to investigate the micro-macro interaction in more detail. We focus on the multilayer regime and limit our study to films with 8 layers and polyanion termination. We report on tailoring the dynamic yield stress by controlling the polyelectrolyte conformation during PEM film assembly. For a specific polyelectrolyte conformation, values of the measured shear stress, σ, can be scaled onto a single master curve. When the polyelectrolytes evolve to brushy conformations, the dynamic yield stress, σ_y, increases dramatically, and we observe a behavior similar to the variation of particle volume fraction, ϕ, or ionic strength of the background fluid, I.

Our results clearly show that the polyelectrolyte conformation is an effective and precise control parameter for the dynamic yield stress.

7.3 Materials and Methods

7.3.1 Materials

We use the layer-by-layer (LbL) self assembly technique [80] to build the PEM films onto self-made polystyrene particles. Contrary to state-of-the-art techniques, LbL self assembly is not restricted to surface charge, size, or shape of the colloidal template. Also, the PEMs can be created from a huge variety of polyanion/polycation and polyelectrolyte/template pairings [4].

Polystyrene Particle Manufacturing and Characterization

Polystyrene (PS) particles were prepared via dispersion polymerization of styrene in ethanol [46], because of the high monodispersity of the samples and the up-scaling ability for the synthesis [49]. Alcohol soluble styrene monomere, initiator, 2,2‘-azobis(2-methylbutyronitrile) (AMBN), stabilizer, poly(vinylpyrrolidone) (PVP K30), and co-stabilizer, Triton X-305, were purchased from Sigma Aldrich and used without further purification. The synthesis route was similar to Song *et al.* [49, 50].

About 80% of the styrene monomere (200 g), stabilizer (PVP K30, 32 g), co-stabilizer (Triton X-305, 11.2 g) and 800 g ethanol were weighed into a 2 l three-neck reaction flask. The filled flask was placed in a 75 °C oil heating bath and permanently stirred at 70 r/min. A starter solution with styrene monomere (40 g) and initiator (AMBN, 8 g) was mixed in a beaker glass and homogenized by a magnetic stirrer, during heating. When the starter solution reached 40 °C, it was poured into the polymerization solution. After 24 hours, the solution was cooled down to room temperature to stop the synthesis.

The particles were washed by centrifugation at 3000 r/min and subsequently decanting the supernatant. Fresh ethanol was added and the washing procedure was repeated 4 times. In a final step, the particles were dried at 30 °C in vacuum, and sieved through a mesh with 20 µm pore size.

The particle size is estimated by dynamic light scattering (Mastersizer 2000, Malvern), which reveals a mean radius $a = 2.5$ µm and a polydispersity of about 3%. The surface charge of the particles, $\zeta = -55$ mV, was determined by electrophoresis experiments (Zetasizer Nano, Malvern). Dry particles were suspended in ultrapure water (Milli-Q, Millipore) at a concentration of 1 g/L to obtain a master suspension. Because the zeta potential measurement suffers from too high particle concentrations, a fraction of the master suspensions was separated and subsequently diluted. The zeta potential was estimated at each dilution step. Values of the

zeta potential became independent of the particle concentration at 10^{-3} g/L and througout this work, the presented zeta potential values were obtained at this concentration.

Polyelectrolyte Multilayer Formation and Characterization

Polyelectrolyte multilayer films with in total 8 layers are assembled onto the PS spheres by consecutively adsorbing polycations, poly(diallyldimethyhlammonium chloride) (PDADMAC), and polyanions, poly(sodiumstyrene sulfonate) (PSS), from aqueous KCl solutions. The used polyelectrolytes, PDADMAC (M_w=100,000-200,000 g/mol, and PSS (M_w=70,000 g/mol) were purchased from Sigma Aldrich and used as recieved. Aqueous deposition solutions of 10^{-2} mol/L polyelectrolyte were prepared by the use of ultrapure water (Milli-Q, Millipore). The deposition solutions were adjusted to the desired ionic strength by adding the desired amount of the monovalent salt KCl.

Polyelectrolyte multilayers were built from the three salt concentrations, $c = 10^{-2}$ mol/L KCl, $c = 5 \cdot 10^{-1}$ mol/L KCl, and $c = 1$ mol/L KCl.

Between the adsorption of successive polyelectrolyte layers, the particles were washed 3 times with polyelectrolyte and salt-free Milli-Q water by centrifugation at 3000 r/min and subsequently decanting and replacing the supernatant. Each adsorbed layer reverses the surface charge of the particles. The charge-reversal was checked by zeta potential measurements (Zetasizer Nano, Malvern), which reveal a zeta potential of about $\zeta = -55$ mV for PSS, and $\zeta = 25$ mV for PDADMAC termination. The PEM modified particles were stored in salt-free Milli-Q water.

Suspension Preparation

Prior to each experiment, we wash the particles three times with the aqueous background fluid, which we adjust to the desired ionic strength, ranging from $I = 10^{-3} - 5 \cdot 10^{-1}$ mol/L KCl. The particles were stored for 24 h at the specific ionic strength [45]. The suspensions were concentrated by sedimentation under gravity and removing the supernatant. Visual inspection of the sedimentation process shows that the occurance of a liquid phase and a particle sediment became apparent at the time scale of days, and hence the samples are stable against sedimentation on the experimental time scale of several hours.

7.3.2 Rheological Setup and Measurement Protocol

A disposable pipette was used to fill in one go about 4 mL of the concentrated suspensions into a concentric cylinder geometry with 0.71 mm gap width. During the experiments, a solvent trap is used to prevent evaporation. Steady shear experiments were performed on a MCR 500 rheometer (Anton Paar), which operates in controlled strain mode. The shear stress response of a decreasing strain rate $\dot{\gamma}$, starting at $1000\,\mathrm{s}^{-1}$, is recorded. In order to enhance the reproducibility, the suspensions were pre-sheared at high strain-rates, $\dot{\gamma} = 500\,\mathrm{s}^{-1}$, to completely erase their mechanical history. At this high strain rate, the viscosity of the suspensions became independent from the strain rate, which indicates that the microstructure is broken down into particles [21]. Subsequently, the suspensions were left at rest for 2 h for the microstructure to rebuild in a reproducible manner.

7.3.3 Aging Protocol

The rejuvenation during pre-shear resets the time, t, of the sample history. Thus, a waiting time $t_w = 7200\,\mathrm{s}$ is necessary to allow the microstructure to rebuild. We use the transient elastic shear modulus, $G'(t)$, to follow this aging during t_w by oscillatory shear (oscillation frequency $\omega = 10\,\mathrm{rad/s}$) with small amplitude, $\gamma_0 = 10^{-2}$. An example is given by Fig.7.2. Similar rejuvenation-aging protocols are proved and tested for the investigation of colloidal suspensions that exhibit yield stress behavior [29, 187–189].

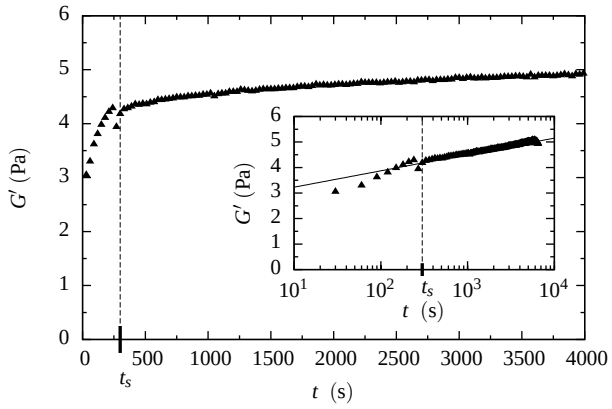

Figure 7.2: Microstructure build up during aging with the transient elastic shear modulus, G', as a function of time, t. The same data are plotted in the inset in semilogarithmic scales, where the solid line is the logarithmic fit to $G'(t)$ for $t > 100\,\mathrm{s}$. The dashed line indicates the structural relaxation time, $t_s = 300\,\mathrm{s}$, at which $G'(t)$ approaches logarithmic behavior.

7.3.4 Discussion on Hershel–Bulkley Model

Because the Hershel–Bulkley (HB) model describes *steady-state* flow curves, we are now interested in the relevant time scales that enter the description of our samples. We found typical viscoelastic relaxation times, η_∞/G_0, of the order of 10^{-3} to 10^{-2} s. We determine the high shear viscosity, η_∞, at $\dot{\gamma} = 500\ \mathrm{s}^{-1}$ in the Newtonian regime of the flow curve. We define the elastic shear modulus, G_0, as the value when $G'(t)$ approaches logarithmic behavior during aging [190]. This is illustrated in Fig. 7.2, where we further define the structural relaxation time, t_s, when $G'(t_s) = G_0$. We like to note that other methods also exist to determine the structural relaxation time [35, 53, 164]. The ratio of the both time scales gives a dimensionless number, $D = \eta_\infty/(G_0 t_s)$, that indicates nonthixotropic materials for D close to unity, and thixotropic materials for $D \ll 1$ [77]. Typical structural relaxation times, t_s of our samples are $t_s < 300$ s. Then, $D < 10^{-4}$ and we deal with thixotropic materials. Hence, we have to validate that a steady-state is reached and we choose a waiting time per measurement point, $t_{wp} = 300$ s, so that $t_{wp} > t_s$ at each imposed strain rate [25, 28, 191, 192].

7.3.5 Volume Fraction Estimation

We estimate the volume fraction from the measured high-shear viscosity [18, 193]

$$\eta_\infty = \eta_f \left(1 - \frac{\phi_{eff}}{\phi_\infty}\right)^{-2} , \tag{7.1}$$

with the background fluid viscosity η_f, the effective, and shear dependent volume fraction, respectively, ϕ_{eff}, and ϕ_∞= 0.71 [136].

The presence of electrostatic or steric interactions, as discussed before, may significantly enlarge the effective particle size, and hence ϕ_{eff}=$(1+\lambda/a)^3\phi$. To evaluate this effect, we use the characteristic length scales λ of both forces, namely the Debye length κ^{-1} and the polymer layer thickness δ. Firstly, we evaluate the Debye length for monovalent salt, $\kappa^{-1} = 0.304\ \mathrm{nm}/\sqrt{I}$, with I denoting the ionic strength of the background fluid [142]. In our experiments, the lowest ionic strength is $I = 10^{-3}$ mol/L KCl, leading to a Debye length $\kappa^{-1}_{max} = 10$ nm. Now we turn to the polymer layer thickness. The largest polymer layer thickness arises in case of brushy polyelectrolyte conformation. Our most brushy (PDADMAC/PSS)$_4$ multilayers, assembled at $c = 1$ mol/L KCl, are about $\delta = 100$ nm thick [44, 45]. The addition of such a relatively thin layer does not significantly increase the effective particle radius. Hence, the effective volume fraction is less than 4% and has no noticeable effect on the rheological properties of the suspensions [194]. Consequently, we estimate all volume fractions by the use of Eqn. (7.1), where we replace ϕ_{eff} by ϕ.

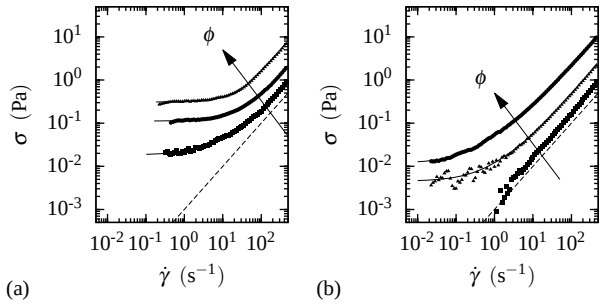

Figure 7.3: Representative flow curves for increasing volume fraction from $\phi \approx 0.2$ over $\phi \approx 0.4$ to $\phi \approx 0.5$ at fixed polyelectrolyte conformation and ionic strength. The plotted data contrast the effect of (a) high, $I = 5 \cdot 10^{-1}$ mol/L KCl, and (b) low, $I = 10^{-3}$ mol/L KCl, ionic strength of the background fluid.

7.4 Results and discussions

By example of Fig. 7.3, we firstly investigate the rheological properties as a function of the volume fraction when the polyelectrolyte conformation and the ionic strength of the background fluid are fixed. Volume fractions ranging from $\phi = 0.1$ to 0.6 were studied. Below a critical volume fraction, $\phi_c \approx 0.2$, the measured shear stress decreases linearly with the applied strain rate, as depicted by the lowest curve in Fig. 7.3(b). Such samples behave Newtonian, with their viscosity exceeding that of the background fluid. This is characteristic for dilute suspensions [18]. Larger volume fractions lead to more complex material behavior, as the recorded shear stress becomes more and more nonlinear at low applied strain rates and finally reaches a plateau value. This kind of material behavior can be modeled as a Herschel-Bulkley (HB) fluid,

$$\sigma(\dot{\gamma}) = \sigma_y + k\dot{\gamma}^n \,, \tag{7.2}$$

with the dynamic yield stress, σ_y, the consistency index, k, and the positive power-law exponent, n, accounting for either shear-thinning, $n < 1$, or -thickening, $n > 1$. The consistency index, k, might be interpreted as an *apparent* viscosity. Fitting Eqn. (7.2) to our rheological data reveals an excellent agreement where σ_y corresponds to the plateau stress, and the exponent correctly captures shear-thinning.

To further investigate the rheological properties, we fix the polyelectrolyte conformation and the particle volume fraction and vary the ionic strength of the background fluid. Comparing Fig. 7.3(a) with Fig. 7.3(b), demonstrates that the ionic strength greatly affects the dynamic yield stress. Values of σ_y drop by one order in response to a reduction of the ionic strength from $I = 5 \cdot 10^{-1}$ mol/L KCl to $I = 10^{-3}$ mol/L KCl.

In conclusion, the data for $\phi > \phi_c$, suggest that the dynamic yield stress behaves similar at different ϕ and I. To compare these data, we scale the measured shear stress, and the applied strain rate, respectively by the scaling factors $\tilde{a}$ and $\tilde{b}$. While the particle loading enhances the viscosity of the samples [18], we have to normalize the horizontal scaling factor $\tilde{b}$ by η_∞. Hence, $\tilde{a}$ and $\tilde{b}/\eta_\infty$ are linearly related, which represents a shift along the viscosity of the background fluid [74]. The scaling factors expand over two decades for brushy PEM films, whereas for flat PEM films they accumulate in a half decade. This much narrower distribution implies that the modification by flat PEM films is less sensitive to the ionic strength of the background fluid.

For each polyelectrolyte conformation, curves of different ϕ and I collapse onto a single master curve, which we exemplarily plot for different brushy PEM films in Fig. 7.4. This figure demonstrates that the modification by brushy PEM films significantly enhances the dynamic yield stress by one order in magnitude.

Remarkably, in Fig. 7.4(a), we observe negative slopes in the $I = 10^{-3}$ mol/L KCl flow curves for the brushy samples at low strain rates. Similar behavior is observed for other soft colloids, like colloidal star polymers, and related to shear banding [25, 188, 195, 196].

The flow curves in Fig. 7.3, together with the master curves in Fig. 7.4, suggest that the fluid changes to a jammed solid, either if the volume fraction or the interparticle interaction exceeds their corresponding critical values $\phi_c \approx 0.2$ or U_c, implying that I is related to the interparticle interaction, U . Thus, the dynamic yield stress denotes the critical stress at the jamming phase boundary, described by $\sigma_y = \sigma_\phi (\phi - \phi_c)^\nu$, where σ_ϕ sets the stress scale of the yield stress, and ν is an exponent which is related to the microstructure of the sample [13]. We focus on high volume fractions, and thus this equation simplifies to [197, 198]

$$\sigma_y = \sigma_\phi \phi^\nu \ . \tag{7.3}$$

As an example, Fig. 7.5(a) shows the dynamic yield stress as a function of the volume fraction for brushy samples. The plotted solid lines denote fits of Eqn. (7.3) to the dynamic yield stress data obtained at ionic strengths between $I = 10^{-3}$ mol/L and $I = 5 \cdot 10^{-1}$ mol/L KCl. As expected from Eqn. (7.3), the dynamic yield stress increases proportional to a constant power of the volume fraction, $\sigma_y \propto \phi^\nu$, with ν=3. Values of ν between 1.4 and 5.5 are typically observed in suspensions of weakly attractive particles that form scale invariant particulate networks [197, 199, 200]. Moreover, Fig. 7.5(a) nicely visualizes the rise of $\sigma_\phi(I)$ with increasing ionic strength, I.

Now we turn to the effect of the polyelectrolyte conformation on the dynamic yield stress. For this, we vary the brushiness, and thus the roughness of the PEM film [178], and plot in Fig. 7.5(b) representative σ_y values at fixed ionic strength, $I = 10^{-1}$ mol/L KCl. Remarkably, values of the dynamic yield stress increase with increasing volume fraction according to $\sigma_y \propto$

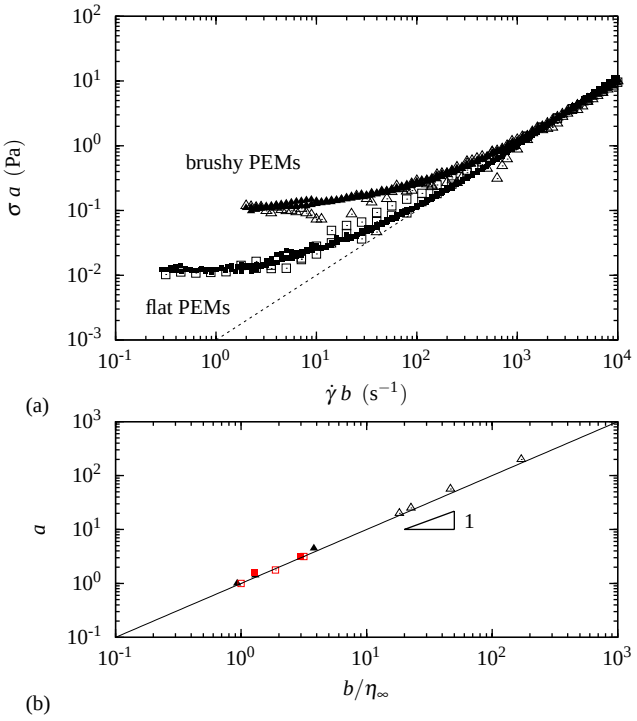

Figure 7.4: (a) Typical curves of normalized shear stress, $\sigma\tilde{a}$, as function of normalized strain rate, $\dot{\gamma}\tilde{b}$, with varying volume fraction ϕ (closed symbols) and ionic strength I (open symbols) of the background fluid. Upper master curve for brushy (triangles), lower for flat (squares) adsorbed polyelectrolytes. The corresponding shift factors are plotted in (b). The open symbols denote values for $I = 10^{-3}$ mol/L KCl, the closed symbols for $I = 10^{-1}$ mol/L KCl. For each polyelectrolyte conformation, the dynamic yield stress value at ϕ=0.60 sets the reference for the shifts.

ϕ^3. Furthermore, σ_ϕ(brushiness), increases with increasing brushiness. Surprisingly, at low and high ionic strength, $I = 10^{-3}$ and $I = 5 \cdot 10^{-1}$ mol/L KCl, the brushiness plays a minor role and values of $\sigma_\phi(brushiness)$ of the different polyelectrolyte conformations are approximately equal.

Firstly, we will discuss the effect of I on σ_ϕ. Using the surface force apparatus (SFA), the dominating interactions between PEMs assembled at high, ≥ 0.5 mol/L, monovalent salt concentration, were recently investigated at fixed polyelectrolyte conformation as a function of the ionic strength of the background fluid [201–203]. These experiments reveal the dominance of steric interactions above $I \approx 10^{-3}$ mol/L, which is the lowest ionic strength we used herein. A finding that is supported by colloidal probe-force measurements under similar conditions [94]. The steric interactions originate from tails and loops of the terminating polyelectrolyte that

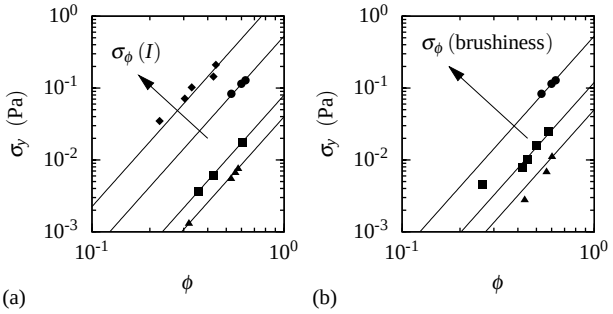

Figure 7.5: Effect of (a) the ionic strength of the background fluid, and (b) polyelectrolyte conformation on the dynamic yield stress. Values of the ionic strength in (a) are $I = 10^{-3}$ mol/L (triangles), $I = 10^{-2}$ mol/L (squares), $I = 10^{-1}$ mol/L (circles), and $I = 5 \cdot 10^{-1}$ mol/L (diamonds) KCl. The measurements in (b) are performed at $I = 10^{-1}$ mol/L KCl, illustrating the evolution from flat to brushy polyelectrolyte conformations. The increase in brushiness is denoted with triangles (flat) over squares to circles (brushy). In both figures, solid lines are fits to the data with the slope 3.

expand from the PEM surface into the surrounding solution. Thus, we can think of the steric layer as a hairy corona around the PEM coated colloids. Recent experiments performed with the support of the osmotic stress technique arrived at the same solid core-PEM shell-hairy corona picture [204].

We expect, that the ionic strength of the background fluid directly influences the steric layer [204]. In a first approximation, we hypothesize that the terminating layer behaves similar to polyelectrolyte brushes. Polyelectrolyte brushes shrink with decreasing ionic strength of the background fluid [157, 205], $\propto I^{-1/3}$. Hence, we anticipate that the steric layer is most extended at low I. Then, the expanding polyelectrolyte chains are experienced to electrostatic self-repulsion, which tends to stretch the polyelectrolyte chains and is balanced by their elasticity. Increasing I leads to an imbalance which results in chain softening and lastly in a collapse of the hairy corona. We speculate that thereby the effective interparticle attraction increases.

The interactions of polyelectrolyte brushes are strongly correlated to the thickness, L, of the brushy layer. The brush thickness is proportional to the decay length of the steric repulsion and hence, we expect the effective attraction [206], $U \propto L^{-1}$. Increasing the ionic strength of the background fluid, I, collapses the brush according to $L \propto (Is^2)^{-1/3}$, where s^2 is often related to the chain length of polyelectrolyte brushes [92, 206]. Herein, we pragmatically use s as a dimensionless shift factor. Using Eqn. (7.3) together with the scaling [200]

$$\sigma_y \propto \frac{U\phi^\nu}{a^2} \,, \tag{7.4}$$

recently proposed for weakly attractive particles with ν close to 3, relates the extra stress to

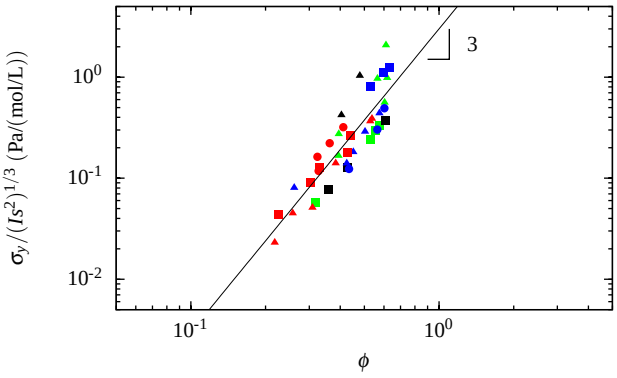

Figure 7.6: (Color) Scaling of the normalized dynamic yield stress, $\sigma_y/(Is^2)^{1/3}$, as a function of particle volume fraction, ϕ. The plotted data are obtained for increasing brushiness, or roughness, from triangles (flat) over squares to circles (brushy) at different ionic strength of the background fluid, visualized by the colors with green ($I = 10^{-3}$ mol/L KCl), black ($I = 10^{-2}$ mol/L KCl), blue ($I = 10^{-1}$ mol/L KCl), and red ($I = 5 \cdot 10^{-1}$ mol/L KCl). Please note that data for $I = 5 \cdot 10^{-1}$ mol/L KCl are not shifted.

the interparticle interactions, $\sigma_\phi \propto U$. Hence, we expect the normalized yield stress to scale as $\sigma_y/(Is^2)^{1/3} \propto \phi^3$, which we plot in Fig. 7.6(a). Remarkably, samples up to $I = 10^{-1}$ mol/L KCl follow this scaling and collapse onto the *unshifted* data for $I = 5 \cdot 10^{-1}$ mol/L KCl. We hypothesize that at this high ionic strength, $I = 5 \cdot 10^{-1}$ mol/L KCl, charges of the hairy layer are largely neutralized and the interactions become dominated by non-specific interactions such as bridging [207, 208] .

Based on Fig. 7.6, we discuss the effect of brushiness, and hence PEM film roughness [178], on σ_ϕ. We estimate $s = 0.01$, 0.04, and 0.1, ordering from flat to brushy adsorbed polyelectrolytes. This corresponds to increasing PEM film roughness [178], visualized by Fig. AFM. The increasing PEM film roughness leads to rising attractive interparticle interactions [94], which is in good accordance to our observed increasing values of s, and hence σ_ϕ. Our findings are also in good qualitative agreement with colloidal probe force measurements [92] as well as yield stress measurements [209, 210] on brushy, or rough, polyelectrolyte monolayers.

7.5 Conclusions

We demonstrate that control over the polyelectrolyte conformation of PEM films serves as a versatile tuning parameter for the dynamic yield stress of colloidal suspensions. Using this tuning parameter opens up the possibility to tailor the dynamic yield stress independently of the physicochemical composition of the background fluid. We show that PEM films consisting of brushy polyelectrolytes give higher dynamic yield stress values. Moreover, the increase of the dynamic yield stress with the evolution from flat to brushy PEM films is similar to that with increasing ionic strength of the background fluid; both effects increase the strength of the interaction energy. Using simple scaling arguments, we draw a first picture of the interaction mechanisms that motivate further studies. Our results show that well-defined, homogeneous polyelectrolyte multilayers are a promising method for the design of colloidal suspensions.

Bibliography

[1] E. M. Mateescu, C. Jeppesen and P. Pincus, *Europhys. Lett.*, 1999, **46**, 493–498.

[2] R. Messina, *J. Phys.: Condens. Matter*, 2009, **21**, 113102–113102.

[3] G. Decher, J. D. Hong and J. Schmitt, *Thin Solid Films*, 1992, **210-211**, 831–835.

[4] G. Decher, J. B. Schlenoff, Decher G., D. G. and S. JB., *Multilayer Thin Films: sequential assembly of nanocomposite materials*, Wiley-VCH, 2003, p. 524.

[5] F. Caruso, H. Lichtenfeld, M. Giersig and H. Möhwald, *J. Am. Chem. Soc.*, 1998, **120**, 8523–8524.

[6] N. Kato, P. Schuetz, A. Fery and F. Caruso, *Macromolecules*, 2002, **35**, 9780–9787.

[7] R. Messina, C. Holm and K. Kremer, *Langmuir*, 2003, **19**, 4473–4482.

[8] G. Schneider and G. Decher, *Nano Lett.*, 2004, **4**, 1833–1839.

[9] J. J. Stickel and R. L. Powell, *Annu. Rev. Fluid Mech.*, 2005, **37**, 129–149.

[10] Liu A. J. and S. R. Nagel, *Jamming and Rheology*, Taylor & Francis, New York, 2001.

[11] G. Biroli, *Nature Phys.*, 2007, **3**, 222–223.

[12] H. A. Barnes and K. Walters, *Rheol. Acta*, 1985, **24**, 323–326.

[13] V. Trappe, V. Prasad, L. Cipelletti, P. N. Segre and D. A. Weitz, *Nature*, 2001, **411**, 772–775.

[14] P. C. F. Mø ller, J. Mewis and D. Bonn, *Soft Matter*, 2006, **2**, 274–283.

[15] P. C. F. Mø ller, D. Bonn and A. Fall, *Europhys. Lett.*, 2009, **87**, 38004–38010.

[16] L. H. P. Fernandez, A. Ott, P. A. Pullarkat, N. Aksel, *A biological cell monolayer shearing apparatus for diagnostic purposes*, 2007.

[17] P. Fernández, L. Heymann, A. Ott, N. Aksel and P. A. Pullarkat, *New*, 2007, **9**, 419.

[18] R. G. Larson, *The Structure and Rheology of Complex Fluids*, Oxford University Press, New York, 1999.

[19] D. Distler, *Wässrige Polymerdispersionen*, Wiley-VCH, Weinheim, 1999.

[20] N. J. Wagner and J. W. Bender, *MRS Bulletin*, 2004, **29**, 100–106.

[21] R. G. Larson, *The Structure and Rheology of Complex Fluids*, Oxford University Press, New York, 1998.

[22] R. M. Davies, *Proceedings of the Royal Society A: Mathematical, Physical and Engineering Sciences*, 1949, **197**, 416–432.

[23] D. C.-H. Cheng, *Rheol. Acta*, 1986, **25**, 542–554.

[24] H. A. Barnes, *J. Non-Newton Fluid Mech.*, 1997, **70**, 1–33.

[25] L. Heymann and N. Aksel, *Phys. Rev. E*, 2007, **75**, 21505–21509.

[26] R. Christensen, *Theory of Viscoelasticity*, Dover Publications, New York, 2003.

[27] T. G. Mezger, *The Rheology Handbook: For Users of Rotational and Oscillatory Rheometers*, Vincentz Network, Hannover, 2006.

[28] L. Heymann, S. Peukert and N. Aksel, *J. Rheol.*, 2002, **46**, 93–112.

[29] K. N. Pham, G. Petekidis, D. Vlassopoulos, S. U. Egelhaaf, W. C. K. Poon and P. N. Pusey, *J. Rheol.*, 2008, **52**, 649–676.

[30] A. Y. Malkin, *Rheol. Acta*, 1995, **34**, 27–39.

[31] A. J. Giacomin and J. M. Dealy, in *Techniques in Rheological Measurements*, ed. C. A. A., Chapman and Hall, 1993, ch. 4, pp. 99 – 121.

[32] M. Wilhelm, D. Maring and H.-W. Spiess, *Rheol. Acta*, 1998, **37**, 399–405.

[33] K. S. Cho, K. Hyun, K. H. Ahn and S. J. Lee, *J. Rheol.*, 2005, **49**, 747–758.

[34] R. H. Ewoldt, A. E. Hosoi and G. H. McKinley, *J. Rheol.*, 2008, **52**, 1427–1458.

[35] H. M. Wyss, K. Miyazaki, J. Mattsson, Z. Hu, D. R. Reichman and D. A. Weitz, *Phys. Rev. Lett.*, 2007, **98**, 238303–238306.

[36] H.-J. Butt, B. Cappella and M. Kappl, *Surf. Sci. Rep.*, 2005, **59**, 1–152.

[37] W. B. Russel, D. A. Saville, W. R. Schowalter, W. B Russel, D. A Saville and W. R Schowalter, *Colloidal Dispersions*, Cambridge University Press, New York, 1989.

[38] J. N. Israelachvili, *Intermolecular and Surface Forces*, Academic Press, London, New York, 1992, vol. 3.

[39] H. Ohshima, *Adv. Colloid Interfac.*, 1995, **62**, 189–235.

[40] H. C. Hulst, *Light Scattering by Small Particles*, Courier Dover Publications, Dover, 1957, p. 470.

[41] C. F. Bohren and D. R. Huffman, *Absorption and Scattering of Light by Small Particles*, Wiley-VCH Verlag GmbH, Weinheim, Germany, 1998.

[42] M. Schönhoff, *Curr. Opin. Colloid In.*, 2003, **8**, 86–95.

[43] K. Ariga, J. P. Hill and Q. Ji, *Phys. Chem. Chem. Phys.*, 2007, **9**, 2319–2340.

[44] S. T. Dubas and J. B. Schlenoff, *Macromolecules*, 1999, **32**, 8153–8160.

[45] S. T. Dubas and J. B. Schlenoff, *Langmuir*, 2001, **17**, 7725–7727.

[46] K. P. Lok and C. K. Ober, *Can. J. Chemistry*, 1985, **63**, 209–216.

[47] C. M. Tseng, Y. Y. Lu, M. S. El-Aasser and J. W. Vanderhoff, *J. Polym. Sci. A1*, 1986, **24**, 2995–3007.

[48] A. J. Paine, W. Luymes and J. McNulty, *Macromolecules*, 1990, **23**, 3104–3109.

[49] J.-S. Song, F. Tronc and M. A. Winnik, *J. Am. Chem. Soc.*, 2004, **126**, 6562–6563.

[50] J.-S. Song and M. A. Winnik, *Polymer*, 2006, **47**, 817–825.

[51] A. J. Paine, *J. Colloid Interf. Sci.*, 1990, **138**, 170–181.

[52] N. Hoda and S. Kumar, *J. Rheol.*, 2007, **51**, 799.

[53] P. Sollich, F. Lequeux, P. Hébraud and M. E. Cates, *Phys. Rev. Lett.*, 1997, **78**, 2020–2023.

[54] A. Kowalczyk, B. Hochstein, P. Staehle, N. Willenbacher, B. M. Erwin, S. A. Rogers, M. Cloitre and D. Vlassopoulos, *J. Rheol.*, 2010, **20**, 187–195.

[55] P. H. Mohan and R. Bandyopadhyay, *Phys. Rev. E*, 2008, **77**, 41803.

[56] A. S. Shedge, P. P. Wadgaonkar, A. K. Lele and M. V. Badiger, *J. Polym. Sci. B Polym. Phys.*, 2010, **48**, 1054–1063.

[57] D. Zang, D. Langevin, B. P. Binks and B. Wei, *Phys. Rev. E*, 2010, **81**, 11604.

[58] R. Krishnaswamy, S. Majumdar and A. K. Sood, *Langmuir*, 2007, **23**, 12951–12958.

[59] M. Oliver, T. Kováts, S. M. Mijailovich, J. P. Butler, J. J. Fredberg and G. Lenormand, *Phys. Rev. Lett.*, 2010, **105**, 158102.

[60] B. M. Erwin, M. Cloitre, M. Gauthier and D. Vlassopoulos, *Soft Matter*, 2010, **6**, 2825–2833.

[61] C. Kalelkar, A. Lele and S. Kamble, *Phys. Rev. E*, 2010, **81**, 31401.

[62] K. Miyazaki, H. M. Wyss, D. A. Weitz and D. R. Reichman, *Europhys. Lett.*, 2006, **75**, 915.

[63] J. M. Brader, M. Siebenbürger, M. Ballauff, K. Reinheimer, M. Wilhelm, S. J. Frey, F. Weysser and M. Fuchs, *Phys. Rev. E*, 2010, **82**, 61401.

[64] M. D. Graham, *J. Rheol.*, 1995, **39**, 697–712.

[65] C. O. Klein, H. W. Spiess, A. Calin, C. Balan and M. Wilhelm, *Macromolecules*, 2007, **40**, 4250–4259.

[66] X. Li, S.-Q. Wang and X. Wang, *J. Rheol.*, 2009, **53**, 1255–1274.

[67] K. Atalik and R. Keunings, *J. Non-Newton. Fluid*, 2004, **122**, 107–116.

[68] A. E. Green and R. S. Rivlin, *Arch. Ration. Mech. An.*, 1957, **1**, 1–21.

[69] S. N. Ganeriwala and C. A. Rotz, *Polym. Eng. Sci.*, 1987, **27**, 165–178.

[70] W. Yu, P. Wang and C. Zhou, *J. Rheol.*, 2009, **53**, 215–238.

[71] M. Abramowitz and I. A. Stegun, *Handbook of Mathematical Functions*, Dover Publications, New York, 1970.

[72] V. Carrier and G. Petekidis, *J. Rheol.*, 2009, **53**, 245–273.

[73] J. Ferry, *Viscoelastic Properties of Polymers*, John Wiley, New York, 1980.

[74] V. Trappe and D. A. Weitz, *Phys. Rev. Lett.*, 2000, **85**, 449–452.

[75] E. E. Pashkovski, J. G. Masters and A. Mehreteab, *Langmuir*, 2003, **19**, 3589–3595.

[76] V. Gopalakrishnan and C. F. Zukoski, *J. Rheol.*, 2007, **51**, 623–644.

[77] P. Coussot and G. Ovarlez, *Eur. Phys. J. E*, 2010, **33**, 183–188.

[78] R. H. Ewoldt, P. Winter, J. Maxey and G. H. McKinley, *Rheol. Acta*, 2010, **49**, 191–212.

[79] R. H. Ewoldt and G. H. McKinley, *Rheol. Acta*, 2010, **49**, 213–219.

[80] G. Decher, *Science*, 1997, **277**, 1232–1237.

[81] F. Caruso, *Adv. Mater.*, 2001, **13**, 11–22.

[82] D. B. Genovese, J. E. Lozano and M. A. Rao, *J. Food. Sci.*, 2007, **72**, 11–20.

[83] D. F. Evans and H. k. Wennerström, *The Colloidal Domain: Where Physics, Chemistry, Biology, and Technology Meet*, Wiley-VCH, Weinheim, 1999, vol. null.

[84] W. J. Frith, T. A. Strivens and J. Mewis, *J. Colloid. Interf. Sci.*, 1990, **139**, 55–62.

[85] D.-M. Liu and W. J. Tseng, *J. Am. Ceram. Soc.*, 1999, **82**, 2647–2652.

[86] E. Dickinson, *Colloid. Surface. B*, 1999, **2**, 161–176.

[87] R. Lenk and A. Ph. Krivoshchepov, *J. Am. Ceram. Soc.*, 2000, **83**, 273–276.

[88] G. S. Grover and S. G. Bike, *Langmuir*, 1995, **11**, 1807–1812.

[89] P. Mpofu, J. Addai-Mensah and J. Ralston, *Int. J. Miner. Process.*, 2003, **71**, 247–268.

[90] B. Braggs, D. Fornasiero, J. Ralston and R. St. Smart, *Clay. Clay Min.*, 1994, **42**, 123–136.

[91] Z. Adamczyk, B. Jachimska, T. Jasinski, P. Warszynski and M. Wasilewska, *Colloid. Surface. A*, 2009, **343**, 96–103.

[92] S. Block and C. A. Helm, *Phys. Rev. E*, 2007, **76**, 30801–030805.

[93] S. Block and C. A. Helm, *J. Phys. Chem. B*, 2008, **112**, 9318–9327.

[94] V. Bosio, F. Dubreuil, G. Bogdanovic and A. Fery, *Colloid. Surface. A*, 2004, **243**, 147–155.

[95] R. J. Larsen, J.-W. Kim, C. F. Zukoski and D. A. Weitz, *Phys. Rev. E*, 2010, **81**, 11502.

[96] F. Varnik, L. Bocquet and J.-L. Barrat, *J. Chem. Phys.*, 2004, **120**, 2788–2801.

[97] G. Ovarlez, S. Rodts, X. Chateau and P. Coussot, 831–844, 2009.

[98] P. C. F. Mø ller, S. Rodts, M. A. J. Michels and D. Bonn, *Phys. Rev. E*, 2008, **77**, 41507.

[99] T. Divoux, D. Tamarii, C. Barentin and S. Manneville, *Phys. Rev. Lett.*, 2010, **104**, 208301.

[100] S. A. Rogers, D. Vlassopoulos and P. T. Callaghan, *Phys. Rev. Lett.*, 2008, **100**, 128304.

[101] L. B. Chen and C. F. Zukoski, *Phys. Rev. Lett.*, 1990, **65**, 44.

[102] M. E. Fagan and C. F. Zukoski, *J. Rheol.*, 1997, **41**, 373–397.

[103] P. A. Nommensen, M. H. G. Duits, D. van den Ende and J. Mellema, *Phys. Rev. E*, 1999, **59**, 3147–3154.

[104] W. B. Russel and M. C. Grant, *Colloid. Surface. A*, 2000, **161**, 271–282.

[105] V. Prasad, V. Trappe, A. D. Dinsmore, P. N. Segre, L. Cipelletti and D. A. Weitz, *Faraday Discuss.*, 2003, **123**, year.

[106] M. K. Chow and C. F. Zukoski, *J. Rheol.*, 1995, **39**, 33–59.

[107] V. Bosio, *Ph.D. thesis*, University of Potsdam, 2003.

[108] R. v. Klitzing, J. E. Wong, W. Jaeger and R. Steitz, *Curr. Opin. Colloid In.*, 2004, **9**, 158–162.

[109] M. Schoenhoff, V. Ball, A. R. Bausch, C. Dejugnat, N. Delorme, K. Glinel, R. v. Klitzing, R. Steitz and M. Schönhoff, *Colloid. Surface. A*, 2007, **303**, 14–29.

[110] M. Elzbieciak, M. Kolasinska and P. Warszynski, *Colloid. Surface. A*, 2008, **321**, 258–261.

[111] A. Ogawa, H. Yamada, S. Matsuda, K. Okajima and M. Doi, *J. Rheol.*, 1997, **41**, 769–785.

[112] S. C. Tsai, D. Botts and B. Viers, *Particul. Sci. Technol.*, 1989, **7**, 87–95.

[113] D. R. Lide, *Handbook of Chemistry and Physics*, CRC Press, Boca Raton, 1998.

[114] I. Popa, G. Gillies, G. Papastavrou and M. Borkovec, *J. Phys. Chem. B*, 2010, **114**, 3170–3177.

[115] S. J. Miklavic, D. Y. C. Chan, L. R. White and T. W. Healy, *J. Phys. Chem.*, 1994, **98**, 9022–9032.

[116] J. Gregory, *J. Colloid Interf. Sci.*, 1973, **42**, 448–456.

[117] C. F. Hoener, K. A. Allan, A. J. Bard, A. Campion, M. A. Fox, T. E. Mallouk, S. E. Webber and J. M. White, *J. Phys. Chem.*, 1992, **96**, 3812–3817.

[118] H. Senff, W. Richtering, C. Norhausen, A. Weiss and M. Ballauff, *Langmuir*, 1998, **15**, 102–106.

[119] A. Burns, H. Ow and U. Wiesner, *Chem. Soc. Rev.*, 2006, **35**, 1028–1042.

[120] R. Ghosh Chaudhuri and S. Paria, *Chem. Rev.*, 2011, **112**, 2373–2433.

[121] M. Castelnovo and J.-F. Joanny, *Langmuir*, 2000, **16**, 7524–7532.

[122] J. B. Schlenoff, *Langmuir*, 2009, **25**, 14007–14010.

[123] A. M. Lowe and N. L. Abbott, *Chem. Mater.*, 2011, **24**, 746–758.

[124] G. B. Sukhorukov, E. Donath, H. Lichtenfeld, E. Knippel, M. Knippel, A. Budde and H. Möhwald, *Colloid. Surface. A*, 1998, **137**, 253–266.

[125] S. Sivakumar, J. K. Gupta, N. L. Abbott and F. Caruso, *Chem. Mater.*, 2008, **20**, 2063–2065.

[126] E. Donath, G. B. Sukhorukov, F. Caruso, S. A. Davis and H. Möhwald, *Angew. Chem.*

Int. Edit., 1998, **37**, 2202–2205.

[127] G. Schneider and G. Decher, *Langmuir*, 2008, **24**, 1778–1789.

[128] Y. M. Lvov, P. Pattekari, X. Zhang and V. Torchilin, *Langmuir*, 2010, **27**, 1212–1217.

[129] A. V. Sadovoy, M. V. Kiryukhin, G. B. Sukhorukov and M. N. Antipina, *Phys. Chem. Chem. Phys.*, 2011, **13**, 4005 – 4012.

[130] N. A. A. Hess, *Soft Matter (submitted)*, 2012.

[131] A. Hess, M. Pretzl, L. Heymann, A. Fery and N. Aksel, *Phys. Rev. E*, 2011, **84**, 31407–031414.

[132] F. Caruso, H. Lichtenfeld, E. Donath and H. Möhwald, *Macromolecules*, 1999, **32**, 2317–2328.

[133] C. Porcel, P. Lavalle, V. Ball, G. Decher, B. Senger, J.-C. Voegel and P. Schaaf, *Langmuir*, 2006, **22**, 4376–83.

[134] J. B. Schlenoff and S. T. Dubas, *Macromolecules*, 2001, **34**, 592–598.

[135] J. Mewis, W. J. Frith, T. A. Strivens and W. B. Russel, *AIChE J.*, 1989, **35**, 415–422.

[136] D. Quemada, *Eur. Phys. J. - Appl. Phys.*, 1998, **1**, 119–127.

[137] D. R. Foss and J. F. Brady, *J. Fluid Mech.*, 2000, **407**, 167–200.

[138] J. R. Melrose and R. C. Ball, *J. Rheol.*, 2004, **48**, 961.

[139] J. R. Melrose and R. C. Ball, *J. Rheol.*, 2004, **48**, 937.

[140] L. Han, Z. Mao, H. Wuliyasu, J. Wu, X. Gong, Y. Yang and C. Gao, *Langmuir*, 2011, **28**, 193–199.

[141] J. R. Melrose, *Faraday Discuss.*, 2003, **123**, 355–368.

[142] X. Cheng, J. H. McCoy, J. N. Israelachvili and I. Cohen, *Science*, 2011, **333**, 1276–1279.

[143] S. Köstler, A. V. Delgado and V. Ribitsch, *J. Colloid Interf. Sci.*, 2005, **286**, 339–48.

[144] J. Bergenholtz, J. F. Brady and M. Vicic, *J. Fluid Mech.*, 2002, **456**, 239–275.

[145] V. Gopalakrishnan and C. F. Zukoski, *J. Rheol.*, 2004, **48**, 1321–1344.

[146] E. Brown, N. A. Forman, C. S. Orellana, H. Zhang, B. W. Maynor, D. E. Betts, J. M. DeSimone and H. M. Jaeger, *Nat Mater*, 2010, **9**, 220–224.

[147] J. F. Brady and G. Bossis, *J. Fluid Mech.*, 1985, **155**, 105–129.

[148] B. J. Maranzano and N. J. Wagner, *J. Chem. Phys.*, 2001, **114**, 10514–10527.

[149] B. J. Maranzano and N. J. Wagner, *J. Rheol.*, 2001, **45**, 1205–1222.

[150] E. Brown and H. M. Jaeger, *Phys. Rev. Lett.*, 2009, **103**, 86001.

[151] E. Brown and H. M. Jaeger, *Science*, 2011, **333**, 1230–1231.

[152] W. H. Boersma, J. Laven and H. N. Stein, *AIChE J.*, 1990, **36**, 321–332.

[153] W. H. Boersma, P. J. M. Baets, J. Laven and H. N. Stein, *J. Rheol.*, 1991, **35**, 1093–1120.

[154] J. D. Mendelsohn, C. J. Barrett, V. V. Chan, A. J. Pal, A. M. Mayes and M. F. Rubner, *Langmuir*, 2000, **16**, 5017–5023.

[155] A. M. Lehaf, H. H. Hariri and J. B. Schlenoff, *Langmuir*, 2012, **28**, 6348–55.

[156] S. M. Notley, S. Biggs and V. S. J. Craig, *Macromolecules*, 2003, **36**, 2903–2906.

[157] G. H. Fredrickson and P. Pincus, *Langmuir*, 1991, **7**, 786–795.

[158] A. A. Potanin and W. B. Russel, *Phys. Rev. E*, 1995, **52**, 6973–6973.

[159] A. Potanin and W. Russel, *Phys. Rev. E*, 1996, **54**, 6973–6973.

[160] L.-N. Krishnamurthy, N. J. Wagner and J. Mewis, *J. Rheol.*, 2005, **49**, 1347–1360.

[161] M. D. Miller and M. L. Bruening, *Langmuir*, 2004, **20**, 11545–11551.

[162] M. D. Miller and M. L. Bruening, *Chem. Mater.*, 2005, **17**, 5375–5381.

[163] R. Malaisamy and M. L. Bruening, *Langmuir*, 2005, **21**, 10587–92.

[164] A. Hess and N. Aksel, *Phys. Rev. E*, 2011, **84**, 051502–051509.

[165] J. R. Stokes and W. J. Frith, *Soft Matter*, 2008, **4**, 1133–1140.

[166] K. Holmberg, *Handbook of Applied Surface and Colloid Chemistry, Volumes 1-2*, John Wiley & Sons, Chichester, 2002.

[167] J. A. Lewis, *Adv. Funct. Mater.*, 2006, **16**, 2193–2204.

[168] U. Raviv, S. Giasson, N. Kampf, J.-F. Gohy, R. Jerome and J. Klein, *Nature*, 2003, **425**, 163–165.

[169] M. Brust and C. J. Kiely, *Colloid. Surface. A*, 2002, **202**, 175–186.

[170] S.-H. Kim, J.-M. Lim, S.-K. Lee, C.-J. Heo and S.-M. Yang, *Soft Matter*, 2010, **6**, 1092–1110.

[171] A. J. Khopade and F. Caruso, *Langmuir*, 2003, **19**, 6219–6225.

[172] N. Lewinski, V. Colvin and R. Drezek, *Small*, 2008, **4**, 26–49.

[173] A. E. Nel, L. Madler, D. Velegol, T. Xia, E. M. V. Hoek, P. Somasundaran, F. Klaessig, V. Castranova and M. Thompson, *Nat. Mater.*, 2009, **8**, 543–557.

[174] R. A. Sperling and W. J. Parak, *Phil. Trans. R. Soc. A*, 2010, **368**, 1333–1383.

[175] M. A. C. Stuart, W. T. S. Huck, J. Genzer, M. Müller, C. Ober, M. Stamm, G. B. Sukhorukov, I. Szleifer, V. V. Tsukruk, M. Urban, F. Winnik, S. Zauscher, I. Luzinov and S. Minko, *Nat. Mater.*, 2010, **9**, 101–13.

[176] Y. Wang, L. Hosta-Rigau, H. Lomas and F. Caruso, *Phys. Chem. Chem. Phys.*, 2011, **13**, 4782–4801.

[177] N. G. Hoogeveen, M. A. Cohen Stuart, G. J. Fleer and M. R. Böhmer, *Langmuir*, 1996, **12**, 3675–3681.

[178] M. Lösche, J. Schmitt, G. Decher, W. G. Bouwman and K. Kjaer, *Macromolecules*, 1998, **31**, 8893–8906.

[179] A. Fall, J. Paredes and D. Bonn, *Phys. Rev. Lett.*, 2010, **105**, 225502–225506.

[180] R. A. McAloney, M. Sinyor, V. Dudnik and M. C. Goh, *Langmuir*, 2001, **17**, 6655–6663.

[181] U. Voigt, W. Jaeger, G. H. Findenegg and R. v. Klitzing, *J. Phys. Chem. B*, 2003, **107**, 5273–5280.

[182] G. Ladam, P. Schaad, J. C. Voegel, P. Schaaf, G. Decher and F. Cuisinier, *Langmuir*, 1999, **16**, 1249–1255.

[183] P. Nazaran, V. Bosio, W. Jaeger, D. F. Anghel and R. v. Klitzing, *J. Phys. Chem. B*, 2007, **111**, 8572–8581.

[184] M. Cornelsen, C. A. Helm and S. Block, *Macromolecules*, 2010, **43**, 4300–4309.

[185] J. Choi and M. F. Rubner, *Macromolecules*, 2005, **38**, 116–124.

[186] T. Aoki, E. A. Decker and D. McClements, *Food Hydrocolloid.*, 2005, **19**, 209–220.

[187] J. J. Crassous, M. Siebenburger, M. Ballauff, M. Drechsler, D. Hajnal, O. Henrich and M. Fuchs, *J. Chem. Phys.*, 2008, **128**, 204902–204916.

[188] S. A. Rogers, P. T. Callaghan, G. Petekidis and D. Vlassopoulos, *J. Rheol.*, 2010, **54**, 133–158.

[189] M. Laurati, S. U. Egelhaaf and G. Petekidis, *J. Rheol.*, 2011, **55**, 673–706.

[190] T. Divoux, C. Barentin and S. Manneville, *Soft Matter*, 2011, **7**, 9335–9349.

[191] L. Heymann, S. Peukert and N. Aksel, *Rheol. Acta*, 2002, **41**, 307–315.

[192] T. Divoux, C. Barentin and S. Manneville, *Soft Matter*, 2011, **7**, 8409–8418.

[193] C. G. de Kruif, E. M. F. van Iersel, A. Vrij and W. B. Russel, *J. Chem. Phys.*, 1985, **83**, 4717–4725.

[194] A. R. Studart, E. Amstad, M. Antoni and L. J. Gauckler, *J. Am. Ceram. Soc.*, 2006, **89**, 2418–2425.

[195] D. Bonn, P. Coussot, H. T. Huynh, F. Bertrand and G. Debregeas, *Europhys. Lett.*, 2002, **59**, 786.

[196] J. D. Goddard, *Annu. Rev. Fluid Mech.*, 2003, **35**, 113–133.

[197] H. E. King, S. T. Milner, M. Y. Lin, J. P. Singh and T. G. Mason, *Phys. Rev. E*, 2007, **75**, 21403–21423.

[198] R. C. Kramb and C. F. Zukoski, *J. Phys.: Condens. Matter*, 2011, **23**, 35102–35115.

[199] M. Colic, G. V. Franks, M. L. Fisher and F. F. Lange, *Langmuir*, 1997, **13**, 3129–3135.

[200] A. R. Studart, E. Amstad and L. J. Gauckler, *Soft Matter*, 2011, **7**, 6408–6412.

[201] K. Lowack and C. A. Helm, *Macromolecules*, 1998, **31**, 823–833.

[202] E. Blomberg, E. Poptoshev, P. M. Claesson and F. Caruso, *Langmuir*, 2004, **20**, 5432–5438.

[203] E. Blomberg, E. Poptoshev and F. Caruso, *Langmuir*, 2006, **22**, 4153–4157.

[204] M. Dubois, M. Schönhoff, A. Meister, L. Belloni, T. Zemb and H. Möhwald, *Phys. Rev. E*, 2006, **74**, 051402 –051412.

[205] N. A. Kumar and C. Seidel, *Macromolecules*, 2005, **38**, 9341–9350.

[206] S. Block and C. A. Helm, *J. Phys. Chem. B*, 2011, **115**, 7301–7313.

[207] H. Gong, J. Garcia-Turiel, K. Vasilev and O. I. Vinogradova, *Langmuir*, 2005, **21**, 7545–7550.

[208] Y.-K. Leong, *Phys. Chem. Chem. Phys.*, 2007, **9**, 5608–18.

[209] K.-S. Khoo, E.-J. Teh, Y.-K. Leong and B. C. Ong, *Langmuir*, 2009, **25**, 3418–3424.

[210] S. M. Notley and Y.-K. Leong, *Phys. Chem. Chem. Phys.*, 2010, **12**, 10594–10601.

Curriculum Vitae

Education

since 2008		**Colloid and Polymer Science**, Research Doctorate Bayreuth Graduate School of Mathematical and Natural Sciences
2008	**Dipl.-Ing.**	**Applied Mechanics**, Graduate Program Dresden University of Technology
2003	**Dipl.-Ing. (BA)**	**Mechanical Engineering**, Industrial Cooperative Undergraduate Program Stuttgart Baden-Wuerttemberg Cooperative State University

Research Experience

10/2011–today	**Research Associate**, Freiberg University of Mining and Technology
08/2008–09/2011	**Research Associate**, Bayreuth University
07/2007–08/2008	**Research Assistent**, Helmholtz-Zentrum Dresden-Rossendorf
09/2005–06/2006	**Research Assistent**, Dresden University of Technology

Industry Experience

07/2000–09/2003	**Junior Mech. Project Engineer**, Maschinen- & Apparatebau Dieterle GmbH

Reference Research Projects

10/2011–today	**"Fluidic Particle Transport at Interfaces Using Actoric Micro Hairs with Switchable Nanopattern"**, Part of BMBF Project "Micro-Nano-Integration"
08/2008–09/2011	**"Rheology of Polyelectrolyte Multilayer Modified Suspensions"**, Part of DFG Research Unit "Nonlinear Dynamics of Complex Continua"

Journals with Peer Review

ResearcherID: C-4059-2011

Erklärung

Die vorliegende Arbeit wurde von mir selbstständig verfasst und ich habe keine anderen als die angegebenen Hilfsmittel benutzt.

Ferner habe ich nicht versucht, anderweitig mit oder ohne Erfolg eine Dissertation einzureichen oder mich der Doktorprüfung zu unterziehen.

Andreas Hess